Origin of azimuthal seismic anisotropy in oceanic plates and mantle

Thorsten W. Becker [a],[*], Clinton P. Conrad [b], Andrew J. Schaeffer [c], Sergei Lebedev [c]

[a] *Department of Earth Sciences, University of Southern California, Los Angeles, CA, United States*
[b] *Department of Geology and Geophysics, University of Hawai'i at Manoa, United States*
[c] *Geophysics Section, School of Cosmic Physics, Dublin Institute for Advanced Studies, Ireland*

ABSTRACT

Seismic anisotropy is ubiquitous in the Earth's mantle but strongest in its thermo-mechanical boundary layers. Azimuthal anisotropy in the oceanic lithosphere and asthenosphere can be imaged by surface waves and should be particularly straightforward to relate to well-understood plate kinematics and large-scale mantle flow. However, previous studies have come to mixed conclusions as to the depth extent of the applicability of paleo-spreading and mantle flow models of anisotropy, and no simple, globally valid, relationships exist. Here, we show that lattice preferred orientation (LPO) inferred from mantle flow computations produces a plausible global background model for asthenospheric anisotropy underneath oceanic lithosphere. The same is not true for absolute plate motion (APM) models. A ∼200 km thick layer where the flow model LPO matches observations from tomography lies just below the ∼1200 °C isotherm of a half-space cooling model, indicating strong temperature-dependence of the processes that control the development of azimuthal anisotropy. We infer that the depth extent of shear, and hence the thickness of a relatively strong oceanic lithosphere, can be mapped this way. These findings for the background model, and ocean-basin specific deviations from the half-space cooling pattern, are found in all of the three recent and independent tomographic models considered. Further exploration of deviations from the background model may be useful for general studies of oceanic plate formation and dynamics as well as regional-scale tectonic analyses.

© 2014 Elsevier B.V. All rights reserved.

1. Introduction

Observations of seismic anisotropy in the upper mantle provide important constraints on the nature of the lithosphere as well as the morphology and time-integrated dynamics of mantle flow over millions of years. Oceanic plates and the relatively weaker asthenosphere beneath them are particularly promising study subjects. Their tectonic history of deformation is one order of magnitude shorter than that of the continental plates, and readily accessible to plate tectonic reconstructions. Moreover, we expect that oceanic plates are less affected by differentiation and chemical heterogeneity than continental plates, and in this sense can be more simply and quantitatively linked to mantle convection models. We can therefore anticipate that inferences from large-scale geodynamic models, be they of quantitative or conceptual type, should match the imaged patterns of seismic anisotropy in oceanic plate systems quite well. Yet, the origin of azimuthal anisotropy remains debated, even for the oceanic mantle realm.

The full elastic tensor anisotropy that describes seismic wave propagation is usually imaged by means of the tensor entries that are expected if a medium with hexagonal anisotropy is aligned such that the symmetry axis is in the horizontal or vertical orientation (Montagner and Nataf, 1986). The corresponding azimuthal and radial types of anisotropy, respectively, capture much of the signal, even though we know that mantle minerals such as olivine have non-hexagonal crystal symmetry contributions (Montagner and Anderson, 1989; Becker et al., 2006; Mainprice, 2007; Song and Kawakatsu, 2013). Given their sensitivity to different depth intervals within the lithosphere–asthenosphere depth range at different periods, surface waves are most suited for the exploration of the vertical variations of anisotropy in the upper mantle. Azimuthal anisotropy constrained using surface waves is our focus here.

Traditionally, two related causes for observed patterns of azimuthal anisotropy in oceanic plates have been considered (Hess, 1964; Forsyth, 1975; Nishimura and Forsyth, 1989; Montagner and Tanimoto, 1991; Smith et al., 2004; Maggi et al., 2006; Debayle and Ricard, 2013). One is the alignment of the fast propagation orientations of azimuthal anisotropy ("fast axes") within intrinsically anisotropic olivine in a way that reflects relative plate motion at

* Corresponding author. Tel.: +1 (213) 740 8365; fax: +1 (213) 740 8801.
 E-mail address: twb@usc.edu (T.W. Becker).

the time of oceanic lithosphere creation, i.e. paleo-spreading orientations. Paleo-spreading orientations and rates can be inferred by computing the gradient of seafloor ages from magnetic anomalies in a relatively straightforward way (e.g. Conrad and Lithgow-Bertelloni, 2007). The resulting anisotropic fabric may then become "frozen in" once the lithosphere cools sufficiently, away from the spreading center (here used interchangeably with "ridge"). As a consequence, this component is perhaps most important for the shallowest layers above ∼100 km. The anisotropic record of this process may then potentially provide clues about the partitioning between rigid motion with brittle deformation and ductile flow within the lithosphere. This is, for example, suggested by variations in the strength of inferred fossil anisotropy in the relatively slowly spreading Atlantic and the fast spreading Pacific (Gaherty et al., 2004). Compositional variations and possible anisotropic layering are also expected to play a role (Gaherty and Jordan, 1995; Beghein et al., 2014).

The other mechanism that is typically invoked for the generation of azimuthal anisotropy is the alignment of fast propagation orientations with current, or geologically recent, mantle flow (Tanimoto and Anderson, 1984; Nishimura and Forsyth, 1989; Montagner and Tanimoto, 1991; Smith et al., 2004; Maggi et al., 2006). The depth dependence of the match between observed azimuthal anisotropy and mantle flow may then allow us to infer the radial extent of a relatively low viscosity, high strain-rate, asthenosphere, or the thickness of the mechanically defined lithosphere on top of it (Nishimura and Forsyth, 1989; Smith et al., 2004; Debayle and Ricard, 2013; Beghein et al., 2014). However, inferring mantle flow with depth is fraught with complexity because of uncertainties in temperature, density, and viscosity variations, which is why absolute plate motion (APM) models are typically considered as a first step. APM models apply plate models of NUVEL (DeMets et al., 1994) type, which provide information about relative plate motions on geological timescales, in some absolute reference frame. The latter can be characterized by different degrees of net rotation of the whole lithosphere with respect to the lower mantle, ranging from zero (no net rotation, NNR) to relatively large values, as in some hotspot reference frames, for example. One can then compare fast axes from imaged azimuthal anisotropy with orientations of plate motions, under the assumption that the mantle at some larger depth is relatively stationary, such that surface velocities are directly related to asthenospheric shear.

While there are pleasingly few geodynamic assumptions involved in APM models, we know that even plate-associated flow alone leads to regional deviations in mantle circulation from the simple shearing that may be expected if the "plate is leading the mantle" (Hager and O'Connell, 1981). Seemingly non-intuitive scenarios where "the mantle is leading the plate", and flowing in directions quite different from plate motions, may, in fact, be widespread (e.g. Long and Becker, 2010; Natarov and Conrad, 2012). Those differences between surface motions and mantle shear are expected to be even more pronounced for additional contributions due to density-driven flow (Hager and Clayton, 1989; Ricard and Vigny, 1989).

Both explanations of imaged anisotropy in terms of paleo-spreading and present-day asthenospheric mantle flow are related to the assumption that it is mainly the lattice preferred orientation (LPO) of intrinsically anisotropic minerals such as olivine in mantle flow that is causing the anisotropy (Nicolas and Christensen, 1987; Zhang and Karato, 1995; Mainprice, 2007). If this is the case, we can model the details of the anisotropic signal that is created by plate tectonics and mantle flow (McKenzie, 1979; Ribe, 1989). This promising link between seismology and geodynamics has motivated a number of first order models of oceanic plate anisotropy derived from mantle flow (e.g. Gaboret

et al., 2003; Becker et al., 2003, 2006, 2008; Behn et al., 2004; Conrad et al., 2007; Conrad and Behn, 2010). If the LPO mechanism is dominant beneath oceanic plates, then any differences in anisotropy strength with depth for different age oceanic lithosphere can fuel further inference, for example on the partitioning between diffusion and dislocation creep (Podolefsky et al., 2004; Becker et al., 2008; Behn et al., 2009). Moreover, the general match of these large-scale models provides credence to the application of mineral physics methods derived from laboratory experiments to nature, such as regional explorations of mantle dynamics and tectonics constrained by seismic anisotropy (e.g. Silver, 1996; Savage, 1999).

If we assume perfect seismological models, complications from the relatively straightforward association between mantle flow, LPO, and seismic anisotropy may still arise in a number of ways, including due to the effects of water (Jung and Karato, 2001) or melt (Holtzman et al., 2003; Kawakatsu et al., 2009). While some mechanisms other than dry, solid LPO, such as high melt-fraction realignment of olivine fabrics, may be limited to certain regions like spreading centers or continental rift zones, volatile content variations in the mantle may be more wide-spread (e.g. Becker et al., 2008; Meier et al., 2009). Further, it is intriguing that recent, global-scale seismological studies have found discrepancies between the imaged azimuthal anisotropy and models of mantle flow, including a pronounced lack of alignment of asthenospheric anisotropy with APM models across broad oceanic regions (Debayle and Ricard, 2013; Burgos et al., 2014; Beghein et al., 2014). Moreover, Song and Kawakatsu (2013) suggested that the entrainment of an orthorhombic asthenospheric layer can explain some of the complexities of subduction zone anisotropy. Whatever the nature of such a layer, it may then also be expected to behave differently than LPO anisotropy formed in mantle flow, further motivating a reexamination of the origin of oceanic mantle azimuthal anisotropy.

Here, we ask the question if these discrepancies between models for and observations of azimuthal anisotropy indicate large-scale differences between oceanic basin dynamics (such as due to their hydration and temperature state), the influence of regional variations in mantle flow operating beneath the plates, or if a general reassessment of the LPO model for anisotropy may be required. This reassessment of azimuthal anisotropy is motivated not only by the inferred incongruities among the LPO-mantle flow models for the origin of anisotropy, but also by dramatic advances in anisotropic imaging in recent years (e.g. Ekström, 2011; Debayle and Ricard, 2013; Schaeffer and Lebedev, 2013b; Yuan and Beghein, 2013; Burgos et al., 2014). For example, recent Rayleigh surface wave models of upper mantle anisotropy have significantly improved in resolution compared to earlier generation v_{SV} models, e.g. those by Debayle et al. (2005) or Lebedev and van der Hilst (2008) (anisotropic signal discussed in Becker et al., 2012) as used in earlier geodynamic studies (Conrad and Behn, 2010; Long and Becker, 2010).

We find that LPO-based anisotropy estimates from mantle flow, rather than APM, do indeed furnish a plausible, global background model of azimuthal anisotropy for oceanic plates and their underlying asthenosphere. How closely this geodynamic background model approximates observed azimuthal anisotropy varies from one oceanic basin to another, and these variations are consistent among different recent anisotropy models. From these comparisons, we infer that anisotropic fabrics below the oceanic thermal boundary layer, as defined by half-space cooling, are well-explained by LPO-induced anisotropy due to mantle shear.
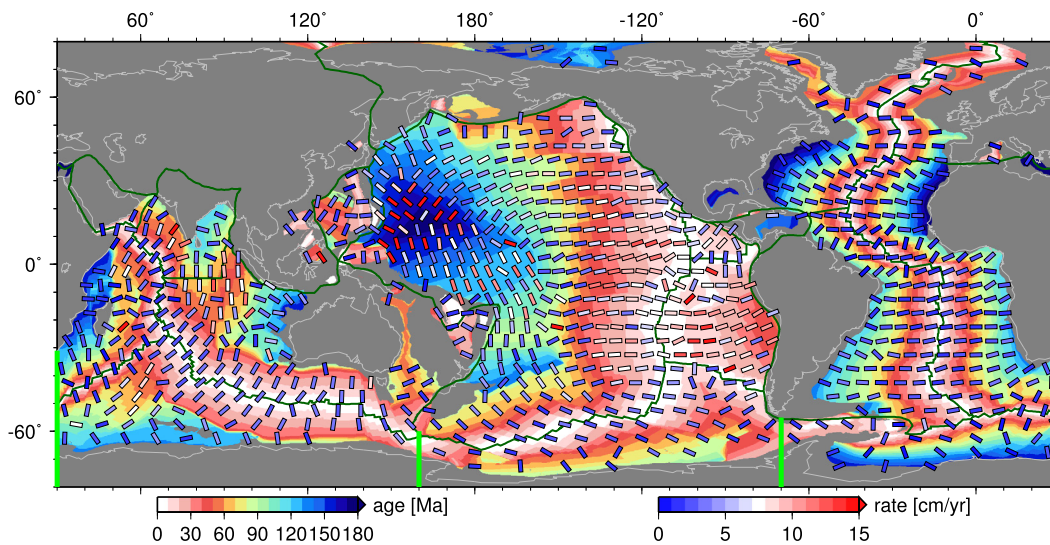
Fig. 1. Seafloor age (from Müller et al., 2008), derived paleo-spreading orientations and rates after $1° \times 1°$ averaging (sticks, colored by rate), plate boundaries (dark green lines, from NUVEL; DeMets et al., 1994), and light green, vertical lines indicating the longitudes used (30°E, 160°E, and 70°W) to subdivide the Antarctic and African plates to define Pacific, Atlantic, and Indian ocean basins. (For interpretation of the references to color in this figure legend, the reader is referred to the web version of this article.)

2. Models

2.1. Seismology

The azimuthal anisotropy of a hexagonally anisotropic medium can be approximated by relative variations in vertically polarized shear waves as

$$\delta v_{SV}(\Psi) = \frac{\Delta v_{SV}}{v_{SV}} \approx A_0 + A_1 \cos(2\Psi) + A_2 \sin(2\Psi). \quad (1)$$

Here, A_i are spatially varying parameters, Ψ indicates the propagation azimuth, and we have assumed that the 2Ψ terms are leading in the full expansion (Montagner and Nataf, 1986). The "fast axis" of maximum v_{SV} propagation is given by $\Psi_{max} = \arctan(A_2/A_1)/2$.

Tomographic imaging using surface waves involves deriving a model of the Earth that is subject to theoretical assumptions about wave propagation, parameterization and regularization choices (e.g. damping in the horizontal and vertical directions), as well as inhomogeneous and imperfect resolution (e.g. Tanimoto and Anderson, 1985; Laske and Masters, 1998; Chevrot and Monteiller, 2009; Ekström, 2011). To illuminate some of the resulting uncertainties, we employ three different tomographic models for comparison to geodynamic predictions of anisotropic fabrics.

We mainly focus our discussions on the recent *SL2013SVA* by Schaeffer and Lebedev (2013b). *SL2013SVA* has high resolution in isotropic structure, but is, by design, relatively smooth in terms of anisotropy. *SL2013SVA* is an *SV* model of the upper mantle, which employs the automated multi-mode waveform inversion technique of Lebedev et al. (2005) and Lebedev and van der Hilst (2008) to accurately extract structural information from surface, *S* and multiple-*S* waveforms. *SL2013SVA* is constructed using the same dataset as *SL2013SV* (Schaeffer and Lebedev, 2013a), comprising waveforms of 522,000 vertical-component seismograms, selected as the most mutually consistent from nearly 750,000 seismograms of the complete, master waveform-fit dataset. Compared to the predecessor (Lebedev and van der Hilst, 2008) this represents more than an order of magnitude increase in the number of waveforms, with the total period range spanning 11–450 s. Further discussion regarding the construction and parameterization of *SL2013SVA* is presented in the Supplementary Material.

We contrast *SL2013SVA* with two other recent works. One is *DR2012* (Debayle and Ricard, 2013), which is also an upper mantle,

azimuthally anisotropic *SV* model. It utilizes an improved separation of the fundamental and first five overtone measurements for Rayleigh waves, compared to the previous version (Debayle et al., 2005), as well as a dataset ∼ four times larger (∼375,000 path-averages) spanning the period range 50–250 s. The other recent model is *YB13SV* (Yuan and Beghein, 2013). This inversion for upper mantle *SV* structure is based on the fundamental mode and overtone phase velocity maps of Visser et al. (2008). It can be considered an end-member in that there is relatively little vertical regularization applied in the inversion, leading to strong changes in azimuthal anisotropy patterns with depth. The relative azimuthal anisotropy patterns, their radial correlation, and cross model comparisons for the three seismological models are further explored in Figs. S1–S3 in the Supplementary Material.

2.2. Geodynamics

The first geodynamic model is based on estimates of paleo-spreading derived from the gradient of seafloor age (Fig. 1), an approach used previously to infer anisotropic fabrics in the oceanic lithosphere (e.g. Smith et al., 2004; Debayle and Ricard, 2013). Our treatment follows that of Conrad and Lithgow-Bertelloni (2007), making sure to first mask out transform faults where local, sharp gradients in seafloor age can lead to artifacts. We then perform a $1 \times 1°$ averaging on the spreading orientations and rates before comparison with azimuthal anisotropy orientations. While spreading rates as computed from the age grids are formally limited to ≤50 cm/yr, the extreme values of rates >20 cm/yr are only reached in very limited regions of the Pacific where the age grid might include interpolation artifacts. In general, 99% of all regions have spreading rates <16 cm/yr (Fig. 1).

For the absolute plate motion models, we always use NUVEL-1A plate relative velocities (DeMets et al., 1994). Plate velocities are also gridded to $1 \times 1°$ before comparisons. As for reference frames, we use no net rotation (model *NNR*), the Pacific hotspot based HS3 model of Gripp and Gordon (2002) (*HS3*), and a newly derived, global ridge-fixed model, ridge no rotation (*RNR*). HS3 differs from NUVEL-1A in that there is a large amplitude (0.44°/Myr) net rotation of the surface velocities with respect to the lower mantle with an Euler pole at 70°E/56°S. This corresponds to a fast drift akin to Pacific plate motions (NNR Euler pole 107°E/63°S) with a global mean amplitude of ≈3.8 cm/yr. Such net rotations would be expected were the hotspots in the Pacific caused by vertical and

stationary plume conduits, and we consider this model's net rotation an end member for hotspot type APM models (Becker, 2008; Kreemer, 2009; Conrad and Behn, 2010; Gérault et al., 2012).

According to tomographic models, azimuthal anisotropy in the asthenosphere beneath large portions of the oceans is oriented with fast-propagation orientations perpendicular to the mid-ocean ridges (e.g. Becker et al., 2012; Debayle and Ricard, 2013; Yuan and Beghein, 2013; Schaeffer and Lebedev, 2013b, Figs. 2b–d). This is consistent with shearing in the oceanic asthenosphere being parallel to the direction of spreading, i.e., perpendicular to the ridge in a reference frame in which the ridge is fixed. Our *RNR* APM model is intended to match these observations by minimizing the motions of the ridges globally in a best-fit sense. We discuss the *RNR* model while realizing that spreading centers are expected to actually move with respect to the deep mantle, particularly if they are passively responding to subduction zone reorganizations. An RNR reference frame can be expected to optimally align plate velocities with the relative spreading direction in the vicinity of the ridges. *RNR* thus complements the paleo-spreading model in that it best represents asthenospheric "spreading" for the present-day. Both *RNR* and paleo-spreading orientations ignore the well-known contribution of density-driven mantle flow beneath the moving plates (e.g. Hager and O'Connell, 1981; Ricard and Vigny, 1989).

We derive *RNR* by fitting a rigid rotation to NNR plate motions from all seafloor with age ≤ 1.5 Ma around the major spreading centers in the three oceanic basins considered (Fig. 1) and subtracting this component from *NNR*. Given these plate kinematics, the resulting globally minimized ridge motion still exhibits some regional ridge migrations. The net rotation component of the *RNR* model (which defines it with respect to NNR) is 0.16°/Myr with an Euler pole at 22°E/82°S (Table S1). This corresponds to $\sim$ purely westward drift at an average velocity of ≈ 1.3 cm/yr. Inversion choices, such as how ridges are weighted, strongly affect the *RNR* Euler pole. However, we refrain from exploring such effects for now, and we also do not seek the APM model which might optimize the fit to seismic anisotropy observations.

In terms of models that attempt to capture actual mantle flow, as opposed to shear inferred from surface motions (e.g. Hager and O'Connell, 1981; Hager and Clayton, 1989; Ricard and Vigny, 1989), we consider two comparable mantle circulation estimates, by Conrad and Behn (2010) and Becker et al. (2008), respectively. Both models incorporate plate motions and the effect of density-driven flow as inferred by scaling seismic tomography to density anomalies. The flow models themselves differ somewhat in their assumptions (Table 1). However, the main difference for the comparison with azimuthal anisotropy is the way that LPO and hence Ψ_{max} from tomography are approximated.

Conrad and Behn's (2010) model uses the infinite strain axes (ISA) orientations as a proxy for fast propagation axes. This quantity was suggested by Kaminski and Ribe (2002) for regions of relatively simple flow ("grain orientation lag", Π, parameter range $\Pi < 0.5$) where fully saturated LPO may be approximated by local velocity gradients, rather than path integration. This *ISA* flow model was optimized by Conrad and Behn (2010) by the ISA match with *SKS* splitting observations at ocean island stations as well as the older azimuthal anisotropy model of Debayle et al. (2005). Here, we only use regions where $\Pi < 0.5$ was inferred by Conrad and Behn (2010) for comparison with tomography, after interpolating the projection of ISA axes onto the horizontal for gridding.

The other mantle flow model is that of Becker et al. (2008) which employs the full kinematic texturing theory of Kaminski et al. (2004) as described in Becker et al. (2006). We use slip systems that yield "A" type LPO fabrics. Those are most abundant in xenolith samples (Mainprice, 2007), and are expected for low stress and relatively low volatile content (Karato et al., 2008). The flow model

includes lateral viscosity variations, forms LPO only in dislocation creep dominated regions (Table 1), and was optimized using the depth-dependent average and lateral patterns of radial anisotropy from Kustowski et al. (2008). This particular *LPO* model was also previously shown to provide a good general geodynamic reference in terms of the match to global radial and azimuthal anisotropy (Becker et al., 2007; Long and Becker, 2010).

2.3. Model performance metrics

To judge how similar models and tomography are, we mainly use the absolute, angular deviation between model and tomography fast axes, $\Delta\alpha$, with $\Delta\alpha \in [0°, 90°]$, since we are comparing orientations rather than directions. In this context, a $\Delta\alpha = 45°$ value indicates random alignment if the two azimuths to be compared are uniformly distributed in α.

When considering global average misfits, we use equal area sampling of those oceanic regions that have defined seafloor age and paleo-spreading rates. From those, we compute a mean misfit after weighing $\Delta\alpha$ by the tomographic anomaly amplitudes in order to down-weigh regions that might be either poorly resolved or have small azimuthal anisotropy. We denote this global mean as $\langle \Delta\alpha \rangle$. Given the difficulty of resolving anisotropic patterns with surface wave inversions, a global, mean angular misfit of $\langle \Delta\alpha \rangle \lesssim 20°$ can be considered an excellent match for a geodynamic model (Becker et al., 2003; Conrad and Behn, 2010; Miller and Becker, 2012). We also comment on correlations, r; in this case, we first expanded all orientational Ψ_{max} fields into generalized spherical harmonics up to spherical harmonic degree $\ell = 20$, setting continental regions to zero, and then compute Pearson's r as in Becker et al. (2007).

Given its area, it is clear that all global metrics will be strongly affected by the behavior of the Pacific plate. This is why we also compute regional misfits for three relatively symmetric subsets, the Pacific basin's Nazca and Pacific plates, the Atlantic's South American and African plates, and the Indian's Australian and Antarctic plates (Fig. 1). The arithmetic mean of these three basin values, $\langle \Delta\alpha \rangle_p$, will be used to give each of these oceanic plate sub-systems equal weight as different expressions of similar geodynamic processes, and we discuss it alongside the simple global $\langle \Delta\alpha \rangle$.

To explore if there are geographic variations in the performance of geodynamic models, such as due to different thermo-chemical states of the asthenosphere, we also subdivide the major oceanic basins into the Pacific (Nazca, Cocos, Pacific, and Antarctic plate), Atlantic (South American, African, North American, Eurasian, Antarctica, and African plate), and Indian basin (Indian, Australian, African, and Antarctic plate), with plate definitions and subdivisions as Fig. 1. While easily reproducible, there are several problems with these regional subsets such as complex tectonics in the Northern Atlantic but we found that different geographic subsets only lead to minor differences in our results.

Lastly, we also discuss model misfit as a function of $\Delta\alpha$ projected into depth, z, and seafloor age, t; for those plots, we compute a mean misfit $\langle \Delta\alpha \rangle_a$ simply based on the interpolated $\Delta\alpha(t, z)$ fields. We compute $\Delta\alpha(t, z)$ for all oceanic plates and when sub-partitioned into the three main oceanic basins as indicated in Fig. 1.

3. Results

3.1. Maps of misfit

Before evaluating the depth, spreading rate, and age dependence of different model fits to imaged azimuthal anisotropy, we discuss a few example misfit maps. Such geographically specific
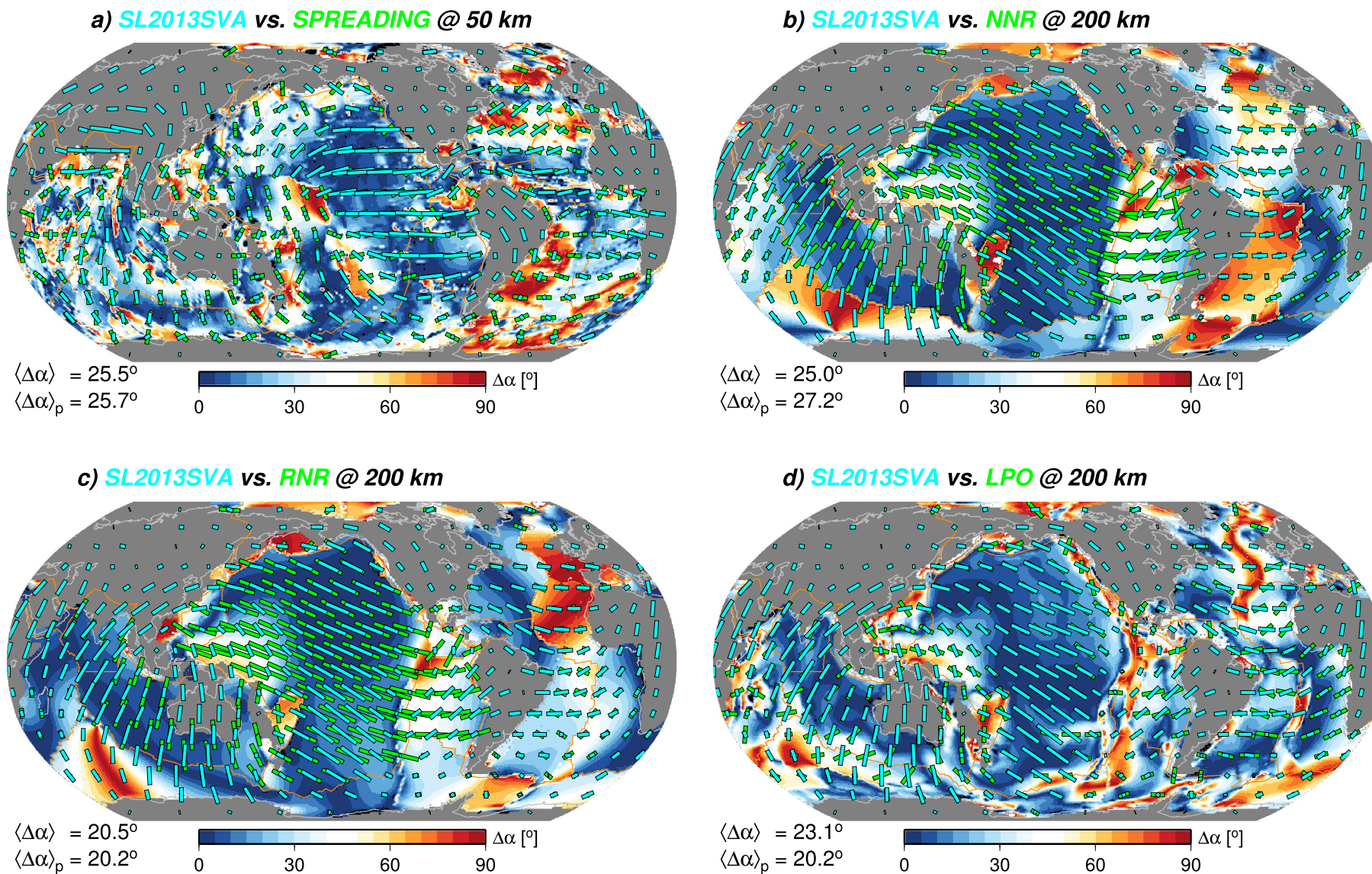
Fig. 2. Comparisons of azimuthal anisotropy (cyan, *SL2013SVA* by Schaeffer and Lebedev, 2013b) with different geodynamic models (green sticks), within lithosphere (50 km, a) and asthenosphere (200 km depth, b–d). a) Paleo-spreading orientations, b) APM model with DeMets et al. (1994) velocities in the no net rotation reference frame (*NNR*), c) APM model with DeMets et al. (1994) velocities in the ridge no rotation (*RNR*) reference frame, and, d) best-fit *LPO* fabric model of Becker et al. (2008) based on mantle flow. Background coloring is the absolute, angular misfit, $\Delta\alpha$; legend specifies the global mean over all basins, $\langle\Delta\alpha\rangle$, and the mean of three basin subset values, $\langle\Delta\alpha\rangle_p$, see text. (For interpretation of the references to color in this figure legend, the reader is referred to the web version of this article.)

Table 1

Comparison of the two geodynamic mantle flow model predictions of azimuthal anisotropy. Similarities between both models include: kinematic surface boundary conditions are relative plate motions from NUVEL-1A (DeMets et al., 1994), tomography velocity anomaly to density scaling of $d\ln\rho/d\ln v_S \approx 0.2$, inclusion of lithospheric thickness variations, and an increase of viscosity between upper and lower mantle of ≈ 50.

|	ISA (Conrad and Behn, 2010)	LPO (Becker et al., 2008)
Reference frame shear	20% of HS3 (Gripp and Gordon, 2002) net rotation	none (NNR)
Density inferred from	S20RTSb (Ritsema et al., 2004)	S362WANI (Kustowski et al., 2008)
Upper thermal boundary layer	excluded from density above 300 km	excluded around cratons
Upper mantle		
Background viscosity, η_{um}	5×10^{20} Pa s, Newtonian	average $\approx 1.8 \times 10^{21}$ Pa s, non-Newtonian
Asthenospheric viscosity	$0.1\eta_{um}$ between base of lithosphere and 300 km	temperature and stress dependent (Becker, 2006)
		$\sim$ three orders of magnitude variations in upper mantle
Velocity gradients	determine anisotropy everywhere	form LPO when in dislocation creep
Method of LPO estimate	ISA axes of Kaminski and Ribe (2002) for $\Pi < 0.5$	full DREX (Kaminski et al., 2004) for A type LPO
Optimization wrt.	SKS splitting and azimuthal anisotropy from Debayle et al. (2005)	radial anisotropy (Kustowski et al., 2008)
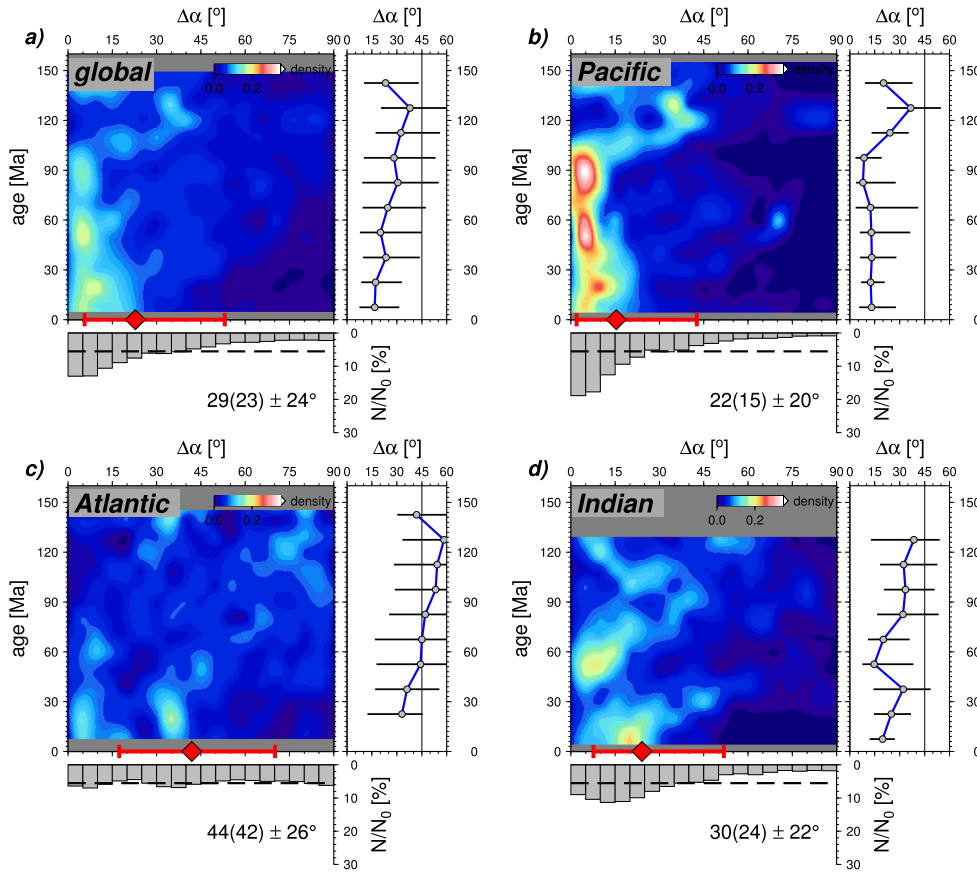
Fig. 3. Age dependence of the angular misfit, $\Delta\alpha$, between azimuthal anisotropy SL2013SVA at lithospheric (50 km) depth and paleo-spreading orientations, as in Fig. 2a; for, a), all regions, b) Pacific, c) Atlantic, and, d), Indian ocean domains (cf. Fig. 1). Colored center plot denotes normalized sampling density (such that each row sums to unity) in $\Delta\alpha$–age space, showing only the y-range which spans the 5–95% quartiles of values sampled. Histogram at bottom shows the distribution of all even-area distributed misfit values within the region, with legend denoting mean (median) ± standard deviation as shown by red bar. Values plotted on right show median ±25 and 75% quartiles for selected age bands, with vertical line denoting the $\Delta\alpha = 45°$ random value. (For interpretation of the references to color in this figure legend, the reader is referred to the web version of this article.)

plots can provide insights as to which geodynamic processes might be captured by the different models, and which may be only poorly approximated. Fig. 2 compares azimuthal anisotropy from SL2013SVA (Schaeffer and Lebedev, 2013b) with different geodynamic models for selected depth ranges.

Fig. 2a shows the match of paleo-spreading with seismology-constrained anisotropy orientations at lithospheric (50 km) depth. It is apparent that this model shows generally a good match to fast axes (global mean of $\langle\Delta\alpha\rangle \approx 25°$), particularly in young seafloor, i.e. close to spreading centers, in the Pacific (Debayle and Ricard, 2013). Parts of the older Pacific, where paleo-spreading directions are quite different from present-day plate motion directions, are,

however, poorly matched (Smith et al., 2004), and the agreement in the Atlantic is worse than in the Pacific.

To examine the age dependence of the match between paleo-spreading direction and azimuthal anisotropy at lithospheric depth, we show sampling density in age–misfit plots (Fig. 3), along with the overall median $\Delta\alpha$ as a function of age. Globally, there is a slight trend toward poorer fits of spreading directions to lithospheric SL2013SVA anisotropy with increasing seafloor age (Fig. 3a), as noted by Debayle and Ricard (2013). Different oceanic basins match spreading directions to varying degrees (Figs. 3b–d); this is broken down into the Pacific region showing consistently good ($\Delta\alpha \lesssim 25°$) fit up to $\sim$100 Ma (cf. Smith et al., 2004), but the
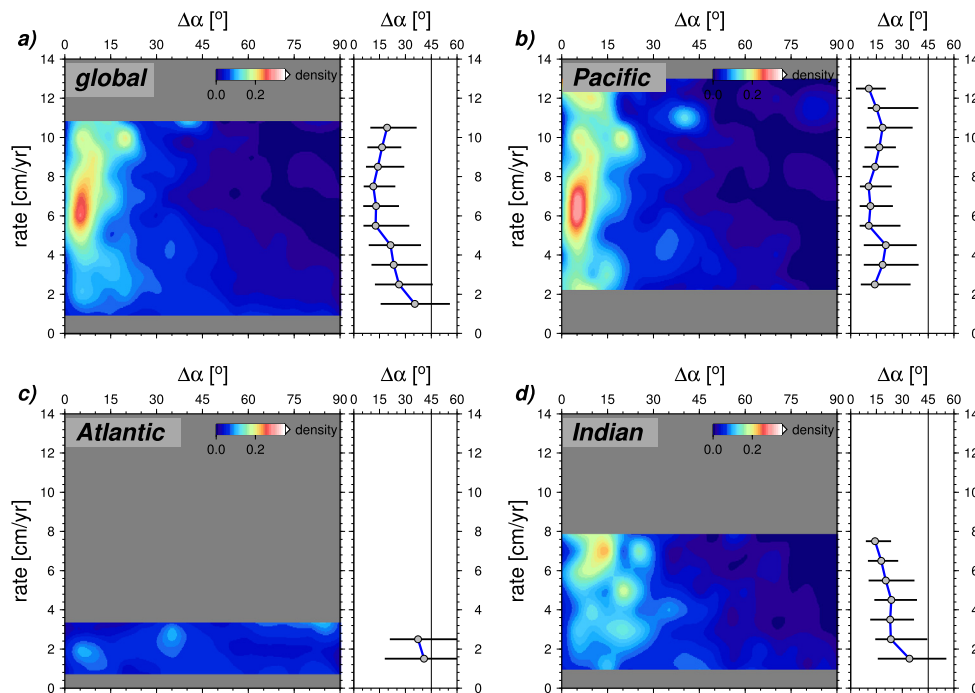
Fig. 4. Paleo-spreading rate dependence of the angular misfit, $\Delta\alpha$, between azimuthal anisotropy *SL2013SVA* at lithospheric (50 km) depth and paleo-spreading orientations, as in Fig. 2a, in analogy to Fig. 3 (see there for detailed caption).

Atlantic is only matching spreading well up to ∼40 Ma (cf. Figs. 1 and 2a).

If we consider the lithospheric misfit with paleo-spreading rate (Fig. 4), we find an indication of a better match between spreading orientations and tomography at spreading rates ≳5 cm/yr, with a clear trend of improved fit with increased spreading in the Indian ocean. While the sampling is perhaps not sufficient to address the physical cause of the observed age and rate trends quantitatively, one interpretation is that relatively fast spreading is required to establish significant azimuthal anisotropy on length-scales that can be detected by surface wave tomography. This may be because the more ubiquitous faulting observed in slower spreading centers, and the associated differences between the partitioning of brittle and ductile lithospheric deformation, leads to less shear-induced LPO formation before the plate cools significantly, for slowly spreading plates (cf. Gaherty et al., 2004).

On top of this rate-dependence, there appears to be a tendency for azimuthal anisotropy beneath older seafloor to not match paleo-spreading well even in the shallowest lithosphere (Fig. 3) (Smith et al., 2004; Maggi et al., 2006; Debayle and Ricard, 2013). This may result from small-scale reheating processes in the bathymetrically anomalous regions of the oceanic lithosphere, such as the Pacific at ages ≳100 Ma (cf. Marty and Cazenave, 1989; Nagihara et al., 1996), perturbing existing shallow LPO fabrics.

For asthenospheric (200 km) depths, the agreement between a no-net-rotation (*NNR*) absolute plate motion model and observed anisotropy is globally comparable to the match of paleo-spreading and anisotropy at shallow, lithospheric depths (cf. Figs. 2a and b). Debayle and Ricard (2013) showed that this agreement between APM models and azimuthal anisotropy within the lithosphere appears to be best in the fastest moving plates, e.g. the Pacific. However, this rate-dependence and the generally convincing global misfit, $\langle\Delta\alpha\rangle$, masks a pronounced geographical misfit pattern, with significant oceanic basin asymmetries between different plates (Fig. 2b). APM alignment for *NNR* provides a good match only for the western, but not eastern, part of the Pacific basin, and the South American plate part of the Atlantic basin is not fit at all. This breakdown of the spreading-center symmetric match of the

paleo-spreading may indicate some deeper mantle flow complexities that the *NNR* APM model cannot easily capture.

When azimuthal anisotropy is compared to the *HS3* APM model (not shown), slightly reduced global misfits at 200 km result, $\langle\Delta\alpha\rangle = 24.3°$ compared to $\langle\Delta\alpha\rangle = 25.1°$ in Fig. 2b for *NNR*. In terms of patterns, *HS3* improves the agreement in the southern Atlantic, but degrades the fit in the African plate, and the Nazca plate region is still not fit. Fig. 2c shows results for the best-fit, ridge-fixed *RNR* model. For this *ad hoc* reference frame, APM alignment at asthenospheric depths is significantly improved from *NNR* in terms of mean misfit; $\langle\Delta\alpha\rangle \approx 20°$. However, regardless of the type of net rotation, no clear geographic patterns of misfit associated with tectonic features arise for any of the APM models, and ocean basin asymmetries exist even for *RNR* (Fig. 2c).

Lastly, Fig. 2d shows the comparison of asthenospheric anisotropy from *SL2013SVA* with the inferred elastic tensor anomalies of the *LPO* model, derived from mantle flow modeling (Becker et al., 2008). Globally, the angular misfit is slightly worse or comparable to *RNR* when computed globally, or basin averaged, respectively. More significantly, the geographic misfit patterns for *LPO* are now again tectonically easily interpretable; most oceanic plate interiors are fit very well, regardless of oceanic basin. However, the *LPO* model does not do a good job in capturing the ridge-proximal regions at asthenospheric depth. This may indicate that reworking of fabrics in the pure-shear, mainly vertical transport domain underneath the ridges may be less well approximated by this particular, steady-state flow model than the mainly simple-shear style plate interiors (Chastel et al., 1993; Blackman and Kendall, 2002; Castelnau et al., 2009). Alternatively, we may see the effect of high partial melt alignment of fabrics (Holtzman et al., 2003) that is not captured by this particular LPO modeling approach.

3.2. Global depth-dependence of misfit

Fig. 5 compares global, oceanic domain model performance with azimuthal anisotropy *SL2013SVA* at uppermost mantle depths, for global mean misfit (Fig. 5a) and when adjusted to weigh each oceanic basin evenly (Fig. 5b). As pointed out above, the alignment
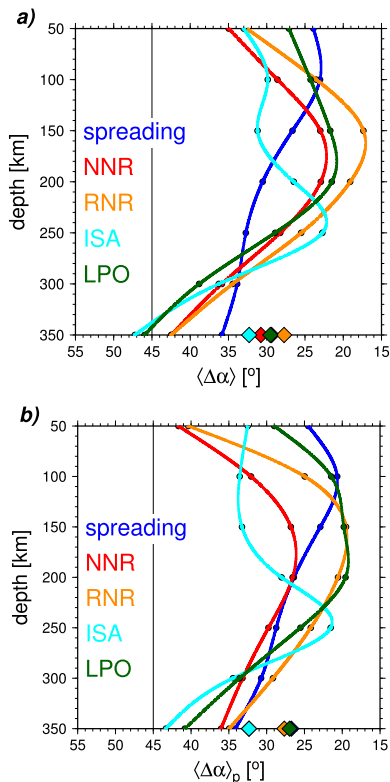
Fig. 5. a) Depth-dependence of global, mean angular misfit, $\langle \Delta\alpha \rangle$, with azimuthal anisotropy in oceanic plates from *SL2013SVA* (Schaeffer and Lebedev, 2013b) (see Figs. S5 and S6 for other models). b) Depth dependence of misfit averaged over three oceanic basin spreading systems, $\langle \Delta\alpha \rangle_p$. Geodynamic models projected downward are paleo-spreading as well as APM models *NNR* and *RNR* (cf. Figs. 2a, b, c). Depth-variable models based on mantle flow considered are *ISA* (Conrad and Behn, 2010) and *LPO* (Becker et al., 2008) (cf. Fig. 2d). Diamonds denote averages over the 50–350 km depth range for each model.

with spreading orientations is best within the lithosphere and continuously deteriorates below. APM models, however, perform more poorly in the lithosphere, and the match with azimuthal anisotropy is best at larger depths of ∼175 km. Without any flow modeling or other assumptions, we may then use the transition depth of ∼125 km based on this transition in Fig. 5a to define an average, global boundary between a cold, presumably mechanically strong lithosphere where anisotropy is frozen in, and the weaker asthenosphere where plate-associated flow causes anisotropy. In detail, this boundary may well be age-dependent, a point to which we return below.

When averaged with depth, the *HS3* APM model leads to a somewhat better match to anisotropy than *NNR*, mainly because of a better match in the lithosphere (not shown). However, this improvement of the comparison between large net rotation surface plate motion models and azimuthal anisotropy at certain depth layers should not necessarily be taken as an argument for the existence of such net rotations. Indeed, when a range of plate motion models with varying amounts of net rotation are imposed above density-driven flow in the mantle, as opposed to a passive mantle, we find that the resulting overall mantle shear is compatible with anisotropy if only moderate amounts of net rotation are included (Becker, 2008; Conrad and Behn, 2010). Reevaluating the new tomography models discussed here in this context fully confirms the findings of Becker (2008); total correlation decreases and angular misfit increases with increasing net rotation component of *LPO* models (Fig. S4).

When considering the *RNR*, stationary spreading center optimized, APM model (Fig. 5), the mean angular misfit is significantly

reduced compared to *NNR*, but the depth dependence is quite similar. If we consider actual mantle flow models, the *ISA* model by Conrad and Behn (2010) leads to a misfit that is generally larger than for the other models, except for depths ∼250 km. This might indicate that the mantle flow model used by Conrad and Behn (2010) less accurately represents aspects of the mantle flow field beneath the oceanic plates. For example, the asthenosphere employed by Conrad and Behn (2010) is ∼200 km thick and uses a Newtonian rheology, whereas Becker et al. (2008) use a ∼300 km thick layer with power-law rheology (Table 1). Alternatively, mantle flow and the generation of anisotropic fabrics may be generally too complex for the ISA to be a good measure of actual LPO caused anisotropy.

The improvement due to one of these two factors is confirmed by considering the *LPO* model from Becker et al. (2008) (Fig. 5). This mantle-flow based estimate of anisotropy generally provides a very good match to tomography at asthenospheric depths, and its performance lies between the APM and spreading models within the lithosphere. This might be expected given that the *LPO* model does not consider changes in plate motions (but see Becker et al., 2003) and is therefore most applicable to flow in the last few Myr (Becker et al., 2006).

Overall, when averaged with depth, the *LPO* model thus performs better than paleo-spreading, and slightly worse (Fig. 5a, $\langle \Delta\alpha \rangle$) or better (Fig. 5b, $\langle \Delta\alpha \rangle_p$) than the best APM model considered, depending on which metric is used. This indicates that LPO formation due to shearing progressing from the pure-shear type upwelling deformation underneath spreading centers to the simple-shear type deformation away from them underneath older lithosphere can be mimicked by *ad hoc* APM models such as *RNR*. However, this deformation is naturally included, in a physically consistent way, in the *LPO* approach based on mantle flow. Together with the tectonically more plausible misfit patterns (Fig. 2), this indicates to us that the *LPO* model is the most plausible explanation for azimuthal anisotropy.

The depth-dependence of the geodynamic model misfit for other tomographic models is comparable to that discussed in Fig. 5 for *SL2013SVA*. For example, considering *DR2012* (Debayle and Ricard, 2013) (Fig. S5), the depth regions in which model fits peak are shifted slightly compared to Fig. 5, but the overall systematics are consistent. The same APM vs. *LPO* systematics hold for *YB13SV* (Yuan and Beghein, 2013) (Fig. S6), though paleo-spreading does not significantly outperform the LPO model even for the lithosphere in that case.

3.3. Model misfit with seafloor age

Given the dynamics of the thermo-chemical processes governing the generation of oceanic seafloor at spreading centers, we expect that the different geodynamic models considered here should show diagnostic behavior with seafloor age when viewed in light of seismic anisotropy. Projecting into age–depth space is perhaps the most useful way of considering misfit when striving to obtain a general understanding of what anisotropy is telling us about how plate tectonics operates.

Half-space cooling is known to control the thermal structure of the oceanic plates (e.g. Davis and Lister, 1974; McKenzie et al., 2005), with some deviations due to thermal resetting where apparent age may not be identical to geological age (Nagihara et al., 1996; Ritzwoller et al., 2004). Seafloor age should therefore also be the main control on the thickness of the rheological boundary layer, and hence affect strain-rate and the depth in which seismic anisotropy is formed by shear alignment (e.g. Podolefsky et al., 2004).

Fig. 6 compares the angular misfit for different geodynamic models and oceanic basins in seafloor age–depth space for the up-
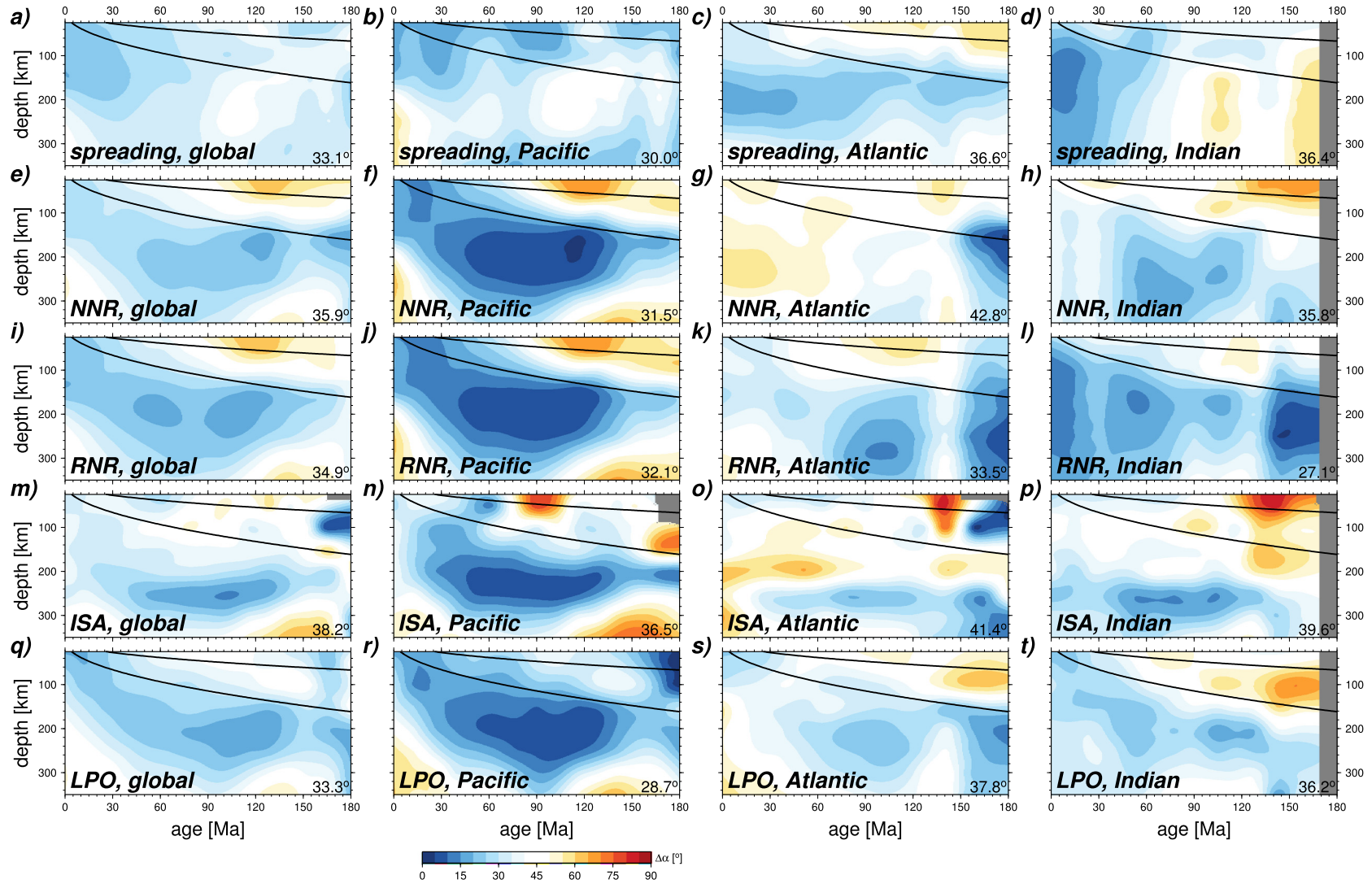
Fig. 6. Angular misfit with azimuthal anisotropy (*SL2013SVA*) compared with paleo-spreading (a–d), *NNR* (e–h) and *RNR* (i–l) APM models, as well as *ISA* (m–p) and *LPO* (q–t) models, for all oceanic plates (1st column), Pacific (2nd column), Atlantic (3rd column), and Indian (4th column) ocean basins. Black contours show 600 and 1200 °C half-space cooling isotherms. Panel average misfit, $\langle\Delta\alpha\rangle_a$, is indicated in the lower right of each panel.

permost mantle. We show 600 °C and 1200 °C isotherms inferred for half-space cooling using temperature-dependent conductivity (Xu et al., 2004), and an asthenospheric temperature of 1315 °C (McKenzie et al., 2005). Analyzing the match of *SL2013SVA* to paleo-spreading directions (top row of Fig. 6) illustrates the depth dependence discussed above (cf. Figs. 3 and 5) and illustrates that spreading orientations at the time of seafloor creation are only a good explanation for the youngest ages, globally speaking.

There are significant differences between the Pacific (where the lithosphere appears to record paleo-spreading) and the Atlantic, where there is some apparent alignment with spreading directions, but most significantly so at asthenospheric rather than lithospheric depths (cf. Fig. 3). This may indicate the effects of relatively slow spreading in the Atlantic (cf. Fig. 4), and/or that asthenospheric flow has been misaligned to relative spreading directions at the surface for the Atlantic for prolonged geological times, leading to incoherent formation of LPO anisotropy throughout the lithosphere. Indeed, young shallow anisotropy in the Atlantic is actually slightly better fit by the *LPO* model that includes both mantle flow and spreading (Fig. 6s) than by the spreading direction itself (Fig. 6c). Alternatively, the discrepancy at lithospheric depths may be due to the weaker LPO development in a relatively narrow Atlantic basin being more difficult for current tomographic models to map accurately.

Considering the alignment with the APM model *NNR* (second row of Fig. 6), it is clear that APM provides a very good explanation for asthenospheric anisotropy in the Pacific. There is some indication that there is an age dependence to part of the match with APM (Debayle and Ricard, 2013). However, there is mainly random alignment underneath the Atlantic (Debayle and Ricard, 2013; Burgos et al., 2014). This calls further into question the general use of APM models as an explanation of uppermost mantle anisotropy underneath and within oceanic plates, even though regionally, and on average, performance of this model is fairly good (Figs. 2b and 5). Even when the well performing, *ad hoc RNR* model is considered (third row of Fig. 6), the misfit plots do not show a uniformly good match to observations, as anticipated.

As for the mantle flow models, Conrad and Behn's (2010) *ISA* (fourth row in Fig. 6) indicates a horizontal streak of well-aligned, asthenospheric anisotropy at ∼275 km (cf. Fig. 5) for the Atlantic and Indian basins, but only the Pacific basin shows any indication of dependence on seafloor age as might be expected based on our understanding of the thermo-mechanical structure of oceanic plates. This may be because of the limited applicability of the ISA approximation to flow-induced LPO textures, or due to the fact that Conrad and Behn's (2010) place the lower-boundary of their low-viscosity asthenospheric layer directly beneath this layer (at 300 km depth), which concentrates shear above it compared to the APM or *LPO* models.

Lastly, the fifth row of Fig. 6 shows the match of Becker et al.'s (2008) *LPO* to *SL2013SVA*. Only this model provides a consistently good ($\Delta\alpha \lesssim 30°$) match to seismic anisotropy, when considered globally and for each of the three oceanic basins, and shows generally the lowest $\langle\Delta\alpha\rangle_a$. More interestingly, the depth extent of the regions of low misfit follows the inferred thermal thickness of the plate from half-space cooling, such that the regions inferred to be hotter than ∼1200 °C are those where the flow models predict anisotropy very well.

4. Discussion

We showed that oceanic azimuthal anisotropy as imaged by Schaeffer and Lebedev (2013b) appears to be consistent with an LPO origin in the uppermost mantle. Moreover, a half-space cooling type temperature dependence provides a good first order estimate of the depth regions where the instantaneous flow model of Becker

et al. (2008) with LPO development provides a good description of observations. In particular, there are no detectable sub-lithospheric layers of decorrelation in Fig. 6, and anisotropy is predicted well underneath the cold lithosphere by *LPO*, irrespective of age. This implies that decoupling layers of the type suggested by Holtzman and Kendall (2010) may not affect plate-scale mantle flow significantly (Becker and Kawakatsu, 2011), may not be detected by surface wave imaging methods, or may not exist. Moreover, this casts some doubts on the interpretation of the match with APM models as being indicative of the extent of mantle flow associated seismic anisotropy, as suggested, for example, by Debayle and Ricard (2013) and Beghein et al. (2014).

Global anisotropic tomography models show less agreement among each other than isotropic tomography (Figs. S1–S3). Also, the regularization dependence of anomaly amplitudes is very pronounced, which is why we focus on fast axes orientations rather than anomaly amplitude here (but see Burgos et al., 2014; Beghein et al., 2014). While most seismological inversions are constructed with comparable theoretical approaches, datasets are different, and in particular different radial damping choices lead to quite different rates of variation of azimuthal anisotropy patterns with depth (Smith et al., 2004; Debayle and Ricard, 2013; Yuan and Beghein, 2013). For example, when expressed as generalized spherical harmonics, the depth-averaged cross-correlations up to $\ell = 8$, $\langle r_8 \rangle$, are 0.57 between *SL2013SVA* (Schaeffer and Lebedev, 2013b) and *DR2012* (Debayle and Ricard, 2013), 0.47 between *SL2013SVA* and *YB13SV* (Yuan and Beghein, 2013) and 0.31 between *DR2012* and *YB13SV* for the uppermost 350 km of the mantle (Fig. S3, cf. Becker et al., 2007). When computed for oceanic plate regions only, the corresponding $\langle r_8 \rangle$ values are improved to 0.63, 0.55, and 0.41, respectively.

This motivates reanalysis of surface wave datasets or, in lieu of that, comparative analysis of different existing models. If we compare the *LPO* model correlation in oceanic plate regions with the different tomographic models, we find $\langle r_8 \rangle$ values of 0.53, 0.42, and 0.41 for *SL2013SVA*, *DR2012*, and *YB13SV*, respectively. This means that the geodynamic *LPO* forward model is as similar to the imaged azimuthal anisotropy as the structural models are among themselves. More instructively, Figs. 7 and 8 repeat the analysis discussed for *SL2013SVA* in Fig. 6 for *DR2012* and *YB13SV*. As can be seen, the details and numerical values of angular misfit are indeed dependent on the seismological model. For example, the reduced vertical damping employed by Yuan and Beghein (2013) appears to be mapped into more horizontally extended patterns (Fig. 8), though even for *YB13SV*, a half-space cooling behavior of the match between LPO and tomography can be detected.

Overall, the general inter-oceanic basin differences, the relative performance of spreading vs. APM vs. *LPO* models, and the trend of consistently low angular misfit below the thermal boundary layer for *LPO* for all oceanic basins, is robust. This suggests that the relationship between anisotropy and tectonics, e.g. the fit to a generically evolving oceanic plate, is now sufficiently well imaged by azimuthal anisotropy tomography to allow more detailed further analysis.

There are a number of uncertainties in mantle flow models, such as the scaling of tomographically imaged wave speed anomalies to temperature or composition, and the spatial distribution of mantle viscosity variations. Indeed, along with global metrics such as the fit to plate motions and geoid anomalies, seismic anisotropy has been used to formally invert for some of these parameters (e.g. Conrad and Behn, 2010; Miller and Becker, 2012). While a formal reassessment of flow model characteristics in light of the improved seismological models is outside the scope of this paper, we have evaluated a set of 75 existing flow models with different density structure and different assumptions on LPO formation in terms of their global misfit. From this analysis, we find
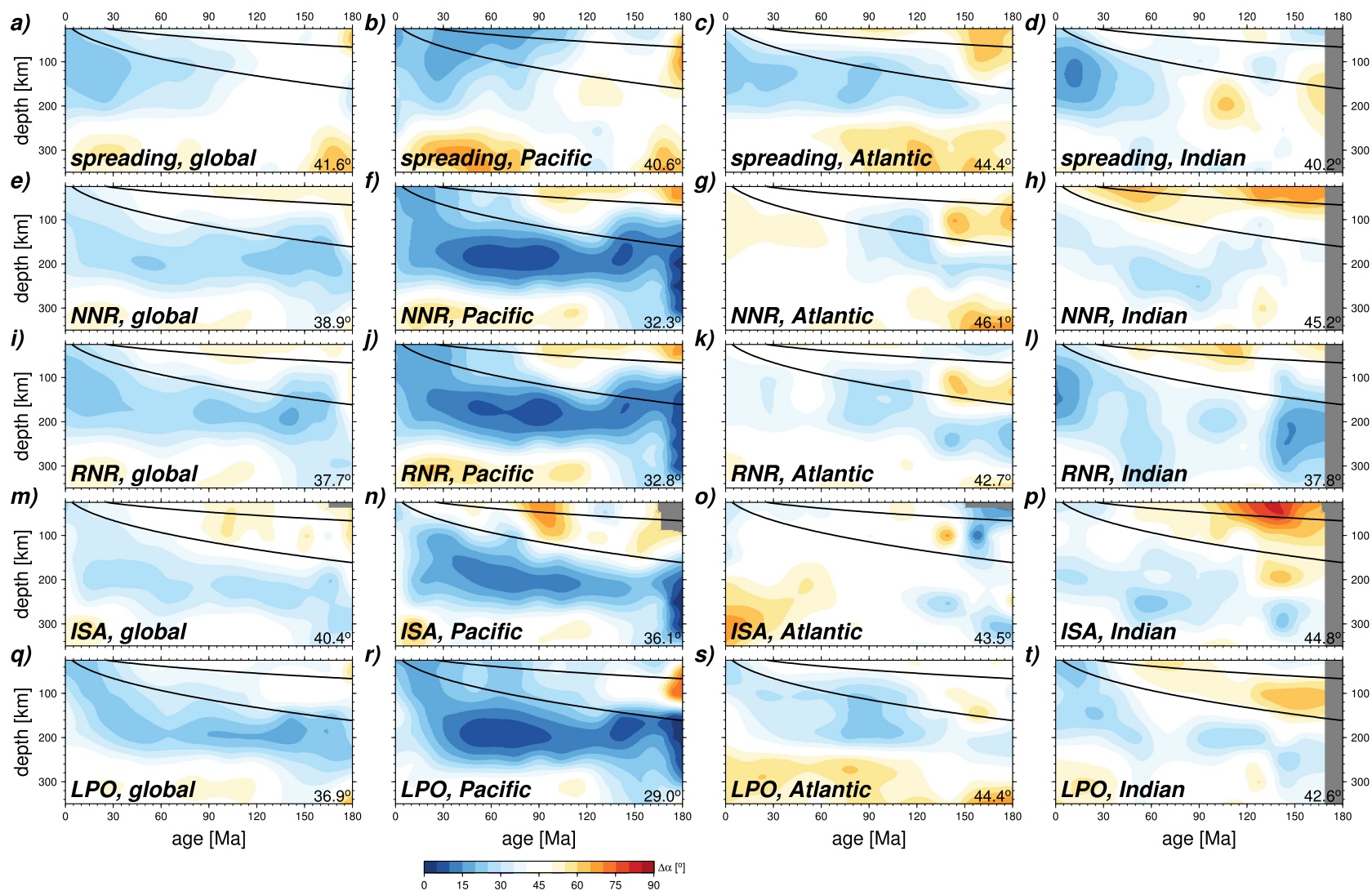
Fig. 7. Angular misfit between models and imaged azimuthal anisotropy from *DR2012* (Debayle and Ricard, 2013) as a function of seafloor age and depth, all else as in Fig. 6, see there for detailed legend.
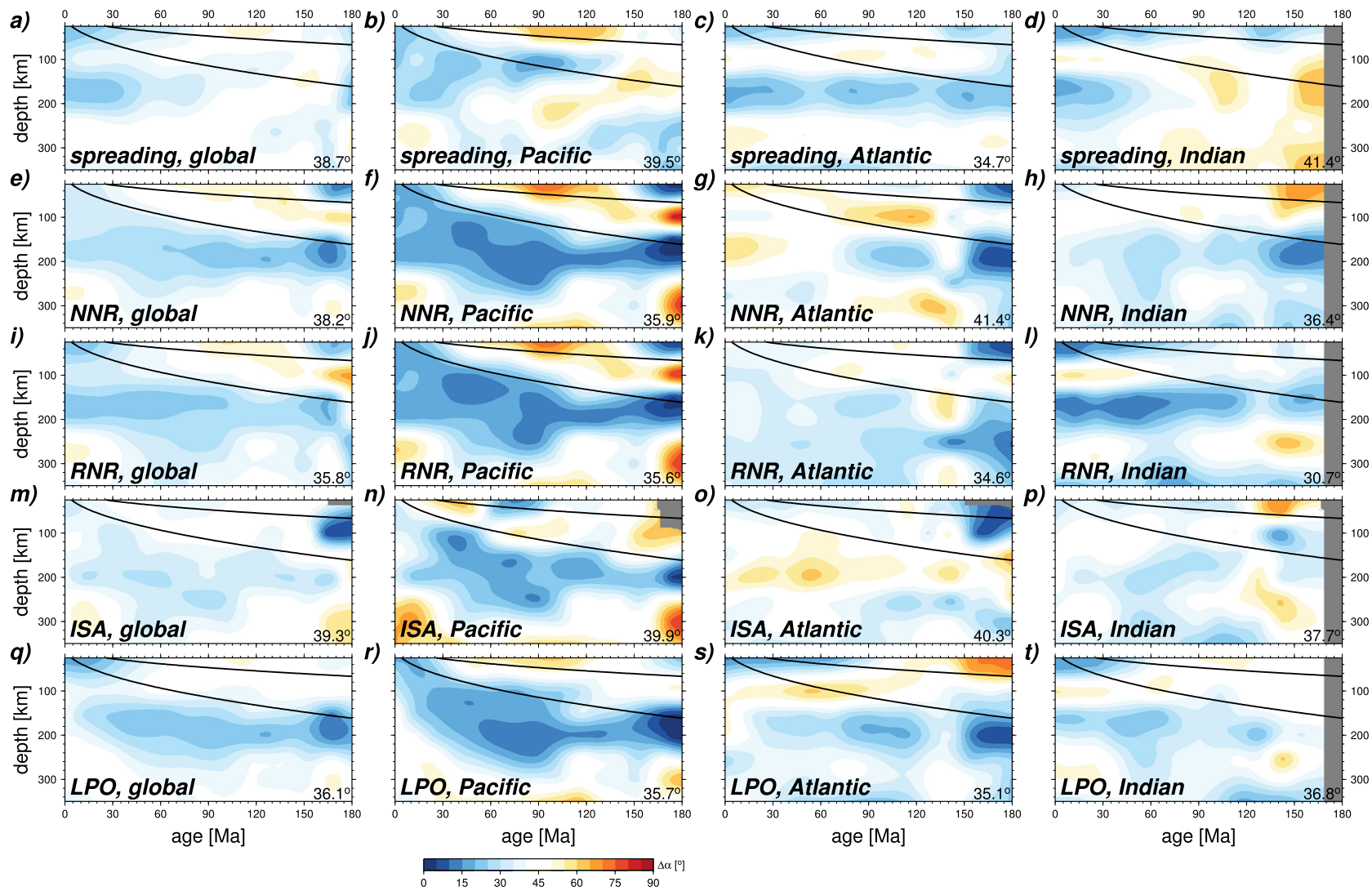
Fig. 8. Angular misfit between models and imaged azimuthal anisotropy from *YB13SV* (Yuan and Beghein, 2013) as a function of seafloor age and depth, all else as in Fig. 6, see there for detailed legend.

that a range of "typical" density models will provide global $\langle r_8 \rangle$ correlations comparable to the best-fit model discussed in this paper. For example, considering the slip systems (Kaminski, 2002; Becker et al., 2008) that give rise to "damp" "E" type, rather than "A" type fabrics (Karato et al., 2008), leads to very similar angular misfits (as mainly amplitudes of anisotropy are affected), but "wet" "C" type would deteriorate the fit.

We therefore expect that detailed refinement of the LPO models, be it by means of adjusting the mantle flow models or by means of refining the treatment of LPO texturing, could possibly improve the match to observations. However, we think that the general finding, that LPO from mantle flow models predicts azimuthal anisotropy below the boundary layer well, and more plausibly than APM models, is robust. Assuming that this is the case, we are left with an interesting conundrum: an LPO origin of azimuthal anisotropy as caused by the shearing of the asthenosphere can be fully explained within compositionally homogeneous mantle flow that is controlled by mechanical strength, as would be inferred from thermal control from a boundary layer. Such an age dependence should then also be reflected in radial anisotropy if caused by the same LPO mechanism, and earlier models did indeed show an increase of the depth of the peak of $\xi = (v_{SH}/v_{SV})^2$ with seafloor age (Nettles and Dziewoński, 2008; Kustowski et al., 2008). While the vertical resolution of ξ remains a challenge, the more recent imaging efforts by Burgos et al. (2014) and Beghein et al. (2014) indicate that such a "lithosphere–asthenosphere boundary" (LAB) in the oceanic basins, as defined by gradients in ξ, may flatten out at very young ages $\lesssim$50 Ma, or show no age-dependence at all.

This discrepancy indicates that effects other than temperature may partially control radial anisotropy, and that other mechanisms such as the shape preferred alignment of partial melt (Kawakatsu et al., 2009; Schmerr, 2012) may have to be invoked to explain the existence of anisotropic layering that is independent of the depth distribution of shear, i.e. strength layering. Put differently, there may be two types of discontinuities in the vicinity of the lithosphere–asthenosphere boundary (cf. Beghein et al., 2014): a structural interface detected by receiver functions (Kawakatsu et al., 2009; Rychert and Shearer, 2009) and underside reflections (Schmerr, 2012) and inferred to be at ∼75 km depth within old oceanic lithosphere, and a mechanical LAB below, as inferred here in light of azimuthal anisotropy and flow modeling, at ∼150 km depth.

5. Conclusions

We confirm that shallow, oceanic-plate azimuthal anisotropy can be explained by frozen-in olivine textures, formed during the generation of oceanic plates. This process is a particularly efficient recorder of paleo-spreading if spreading rates are $\gtrsim$5 cm/yr. In old Pacific seafloor, these original anisotropy patterns appear disrupted, whereas the slowly spreading Atlantic lithosphere shows little apparent correlation between anisotropy and spreading. This is perhaps indicative of persistent relative motions of the uppermost mantle in directions at large angles to relative spreading at the surface.

At asthenospheric depths, absolute plate motion models provide a good formal description for the alignment of azimuthal anisotropy in parts of the oceanic mantle, substantiating earlier results. However, such models yield poor matches to tomographically-inferred anisotropic fabrics across some areas of the ocean basins, perhaps because they utilize a simplified representation of asthenospheric shear that ignores the contribution of mantle flow beneath the surface plate motions. In contrast, mantle flow computations that naturally include the physical processes that produce lattice preferred orientation textures of upper mantle olivine

capture the imaged azimuthal anisotropy globally within the asthenosphere, and to some extent within the shallower oceanic lithosphere as well. Moreover, the geographic distribution of misfit can be understood tectonically: Underneath large oceanic plates, predictions are good; right underneath spreading centers, predictions are poor, perhaps because of intense reworking of fabrics, or because of the effects of partial melt. Thus, except in the vicinity of spreading centers, we conclude that azimuthal anisotropy in the asthenosphere beneath the oceanic lithosphere is well represented by flow models that include plate motions, sublithospheric mantle flow, and LPO-induced anisotropic fabric development.

A good match between anisotropy and flow model predicted *LPO* is found regardless of which oceanic basin or seismological model is considered. The match to the mantle flow model is best within a depth range of ∼200 km, below the ∼1200 °C isotherm as inferred from half-space cooling. This region indicates the depth extent of an asthenospheric shearing layer, as defined based on mechanical properties. The predictions work well for any seafloor age, and there is no indication of mechanical decoupling, or lubrication layers, between asthenosphere and lithosphere, nor is there a need to invoke different mechanisms for several azimuthally anisotropic layers.

Robust patterns in the secondary differences in model fit between oceanic basins may provide further insights, building upon this general geodynamic reference model for oceanic anisotropy. Such efforts may help to advance our understanding of plate formation processes, such as the role of partial melting and chemical differentiation, as well as the effects of later reheating and intraplate deformation.

Appendix A. Supplementary material

Supplementary material related to this article can be found online at http://dx.doi.org/10.1016/j.epsl.2014.06.014.

References

Becker, T.W., 2006. On the effect of temperature and strain-rate dependent viscosity on global mantle flow, net rotation, and plate-driving forces. Geophys. J. Int. 167, 943–957.

Becker, T.W., 2008. Azimuthal seismic anisotropy constrains net rotation of the lithosphere. Geophys. Res. Lett. 35, L05303. http://dx.doi.org/10.1029/2007GL032928. Correction: http://dx.doi.org/10.1029/2008GL033946.

Becker, T.W., Kawakatsu, H., 2011. On the role of anisotropic viscosity for plate-scale flow. Geophys. Res. Lett. 38, L17307. http://dx.doi.org/10.1029/2011GL048584.

Becker, T.W., Kellogg, J.B., Ekström, G., O'Connell, R.J., 2003. Comparison of azimuthal seismic anisotropy from surface waves and finite-strain from global mantle-circulation models. Geophys. J. Int. 155, 696–714.

Becker, T.W., Chevrot, S., Schulte-Pelkum, V., Blackman, D.K., 2006. Statistical properties of seismic anisotropy predicted by upper mantle geodynamic models. J. Geophys. Res. 111, B08309. http://dx.doi.org/10.1029/2005JB004095.

Becker, T.W., Ekström, G., Boschi, L., Woodhouse, J.W., 2007. Length-scales, patterns, and origin of azimuthal seismic anisotropy in the upper mantle as mapped by Rayleigh waves. Geophys. J. Int. 171, 451–462.

Becker, T.W., Kustowski, B., Ekström, G., 2008. Radial seismic anisotropy as a constraint for upper mantle rheology. Earth Planet. Sci. Lett. 267, 213–237.

Becker, T.W., Lebedev, S., Long, M.D., 2012. On the relationship between azimuthal anisotropy from shear wave splitting and surface wave tomography. J. Geophys. Res. 117, B01306. http://dx.doi.org/10.1029/2011JB008705.

Beghein, C., Yuan, K., Schmerr, N., Xing, Z., 2014. Changes in seismic anisotropy shed light on the nature of the Gutenberg discontinuity. Science 343, 1237–1240. http://dx.doi.org/10.1126/science.1246724.

Behn, M.D., Conrad, C.P., Silver, P.G., 2004. Detection of upper mantle flow associated with the African Superplume. Earth Planet. Sci. Lett. 224, 259–274.

Behn, M.D., Hirth, G., Elsenbeck II, J.R., 2009. Implications of grain size evolution on the seismic structure of the oceanic upper mantle. Earth Planet. Sci. Lett. 282, 178–189.

Blackman, D.K., Kendall, J.-M., 2002. Seismic anisotropy of the upper mantle: 2. Predictions for current plate boundary flow models. Geochem. Geophys. Geosyst. 3. http://dx.doi.org/10.1029/2001GC000247.

Burgos, G., Montagner, J.-P., Beucler, E., Capdeville, Y., Mocquet, A., Drilleau, M., 2014. Oceanic lithosphere/asthenosphere boundary from surface wave dispersion data. J. Geophys. Res., 1079–1093. http://dx.doi.org/10.1002/2013JB010528.

Castelnau, O., Blackman, D.K., Becker, T.W., 2009. Numerical simulations of texture development and associated rheological anisotropy in regions of complex mantle flow. Geophys. Res. Lett. 36, L12304. http://dx.doi.org/10.1029/2009GL038027.

Chastel, Y.B., Dawson, P.R., Wenk, H.-R., Bennett, K., 1993. Anisotropic convection with implications for the upper mantle. J. Geophys. Res. 98, 17757–17771.

Chevrot, S., Monteiller, V., 2009. Principles of vectorial tomography – the effects of model parametrization and regularization in tomographic imaging of seismic anisotropy. Geophys. J. Int. 179, 1726–1736.

Conrad, C.P., Behn, M., 2010. Constraints on lithosphere net rotation and asthenospheric viscosity from global mantle flow models and seismic anisotropy. Geochem. Geophys. Geosyst 11, Q05W05. http://dx.doi.org/10.1029/2009GC002970.

Conrad, C.P., Lithgow-Bertelloni, C., 2007. Faster seafloor spreading and lithosphere production during the mid-Cenozoic. Geology 35, 29–32.

Conrad, C.P., Behn, M.D., Silver, P.G., 2007. Global mantle flow and the development of seismic anisotropy: differences between the oceanic and continental upper mantle. J. Geophys. Res. 112, B07317. http://dx.doi.org/10.1029/2006JB004608.

Davis, E.E., Lister, C.R.B., 1974. Fundamentals of ridge crest topography. Earth Planet. Sci. Lett. 21, 405–413.

Debayle, E., Ricard, Y., 2013. Seismic observations of large-scale deformation at the bottom of fast-moving plates. Earth Planet. Sci. Lett. 376, 165–177.

Debayle, E., Kennett, B.L.N., Priestley, K., 2005. Global azimuthal seismic anisotropy and the unique plate-motion deformation of Australia. Nature 433, 509–512.

DeMets, C., Gordon, R.G., Argus, D.F., Stein, S., 1994. Effect of recent revisions to the geomagnetic reversal time scale on estimates of current plate motions. Geophys. Res. Lett. 21, 2191–2194.

Ekström, G., 2011. A global model of Love and Rayleigh surface wave dispersion and anisotropy, 25–250 s. Geophys. J. Int. 187, 1668–1686.

Forsyth, D.W., 1975. The early structural evolution and anisotropy of the oceanic upper mantle. Geophys. J. R. Astron. Soc. 43, 103–162.

Gaboret, C., Forte, A.M., Montagner, J.-P., 2003. The unique dynamics of the Pacific Hemisphere mantle and its signature on seismic anisotropy. Earth Planet. Sci. Lett. 208, 219–233.

Gaherty, J.B., Jordan, T.H., 1995. Lehmann discontinuity as the base of an anisotropic layer beneath continents. Science 268, 1468–1471.

Gaherty, J.B., Lizarralde, D., Collins, J.A., Hirth, G., Kim, S., 2004. Mantle deformation during slow seafloor spreading constrained by observations of seismic anisotropy in the western Atlantic. Earth Planet. Sci. Lett. 228, 225–265.

Gérault, M., Becker, T.W., Kaus, B.J.P., Faccenna, C., Moresi, L.N., Husson, L., 2012. The role of slabs and oceanic plate geometry for the net rotation of the lithosphere, trench motions, and slab return flow. Geochem. Geophys. Geosyst. 13, Q04001. http://dx.doi.org/10.1029/2011GC003934.

Gripp, A.E., Gordon, R.G., 2002. Young tracks of hotspots and current plate velocities. Geophys. J. Int. 150, 321–361.

Hager, B.H., Clayton, R.W., 1989. Constraints on the structure of mantle convection using seismic observations, flow models, and the geoid. In: Peltier, W.R. (Ed.), Mantle Convection: Plate Tectonics and Global Dynamics. In: The Fluid Mechanics of Astrophysics and Geophysics, vol. 4. Gordon and Breach Science Publishers, New York, NY, pp. 657–763.

Hager, B.H., O'Connell, R.J., 1981. A simple global model of plate dynamics and mantle convection. J. Geophys. Res. 86, 4843–4867.

Hess, H.H., 1964. Seismic anisotropy of the uppermost mantle under oceans. Nature 203, 629–631.

Holtzman, B.K., Kendall, J., 2010. Organized melt, seismic anisotropy, and plate boundary lubrication. Geochem. Geophys. Geosyst. 11, Q0AB06. http://dx.doi.org/10.1029/2010GC003296.

Holtzman, B.K., Kohlstedt, D.L., Zimmerman, M.E., Heidelbach, F., Hiraga, T., Hustoft, J., 2003. Melt segregation and strain partitioning: implications for seismic anisotropy and mantle flow. Science 301, 1227–1230.

Jung, H., Karato, S.-i., 2001. Water-induced fabric transitions in olivine. Science 293, 1460–1463.

Kaminski, É., 2002. The influence of water on the development of lattice preferred orientation in olivine aggregates. Geophys. Res. Lett. 29. http://dx.doi.org/10.1029/2002GL014710.

Kaminski, É., Ribe, N.M., 2002. Time scales for the evolution of seismic anisotropy in mantle flow. Geochem. Geophys. Geosyst. 3. http://dx.doi.org/10.1029/2001GC000222.

Kaminski, É., Ribe, N.M., Browaeys, J.T., 2004. D-Rex, a program for calculation of seismic anisotropy due to crystal lattice preferred orientation in the convective upper mantle. Geophys. J. Int. 157, 1–9.

Karato, S.-i., Jung, H., Katayama, I., Skemer, P., 2008. Geodynamic significance of seismic anisotropy of the upper mantle: new insights from laboratory studies. Annu. Rev. Earth Planet. Sci. 36, 59–95.

Kawakatsu, H., Kumar, P., Takei, Y., Shinohara, M., Kanazawa, T., Araki, E., Suyehiro, K., 2009. Seismic evidence for sharp lithosphere–asthenosphere boundaries of oceanic plates. Science 324, 499–502.

Kreemer, C., 2009. Absolute plate motions constrained by shear wave splitting orientations with implications for hot spot motions and mantle flow. J. Geophys. Res. 114, B10405. http://dx.doi.org/10.1029/2009JB006416.

Kustowski, B., Ekström, G., Dziewoński, A.M., 2008. Anisotropic shear-wave velocity structure of the Earth's mantle: a global model. J. Geophys. Res. 113. http://dx.doi.org/10.1029/2007JB005169.

Laske, G., Masters, G., 1998. Surface-wave polarization data and global anisotropic structure. Geophys. J. Int. 132, 508–520.

Lebedev, S., van der Hilst, R.D., 2008. Global upper-mantle tomography with the automated multimode inversion of surface and S-wave forms. Geophys. J. Int. 173, 505–518.

Lebedev, S., Nolet, G., Meier, T., van der Hilst, R.D., 2005. Automated multimode inversion of surface and S waveforms. Geophys. J. Int. 162, 951–964.

Long, M.D., Becker, T.W., 2010. Mantle dynamics and seismic anisotropy. Earth Planet. Sci. Lett. 297, 341–354.

Maggi, A., Debayle, E., Priestley, K., Barruol, G., 2006. Azimuthal anisotropy of the Pacific region. Earth Planet. Sci. Lett. 250, 53–71.

Mainprice, D., 2007. Seismic anisotropy of the deep Earth from a mineral and rock physics perspective. In: Schubert, G., Bercovici, D. (Eds.), Treatise on Geophysics, vol. 2. Elsevier, pp. 437–492.

Marty, J.C., Cazenave, A., 1989. Regional variations in subsidence rate of oceanic plates: a global analysis. Earth Planet. Sci. Lett. 94, 301–315.

McKenzie, D.P., 1979. Finite deformation during fluid flow. Geophys. J. R. Astron. Soc. 58, 689–715.

McKenzie, D., Jackson, J., Priestley, K., 2005. Thermal structure of oceanic and continental lithosphere. Earth Planet. Sci. Lett. 233, 337–349.

Meier, U., Trampert, J., Curtis, A., 2009. Global variations of temperature and water content in the mantle transition zone from higher mode surface waves. Earth Planet. Sci. Lett. 282, 91–101.

Miller, M.S., Becker, T.W., 2012. Mantle flow deflected by interactions between subducted slabs and cratonic keels. Nat. Geosci. 5, 726–730.

Montagner, J.-P., Anderson, D.L., 1989. Petrological constraints on seismic anisotropy. Phys. Earth Planet. Inter. 54, 82–105.

Montagner, J.-P., Nataf, H.-C., 1986. A simple method for inverting the azimuthal anisotropy of surface waves. J. Geophys. Res. 91, 511–520.

Montagner, J.-P., Tanimoto, T., 1991. Global upper mantle tomography of seismic velocities and anisotropies. J. Geophys. Res. 96, 20337–20351.

Müller, R.D., Sdrolias, M., Gaina, C., Roest, W.R., 2008. Age, spreading rates and spreading asymmetry of the world's ocean crust. Geochem. Geophys. Geosyst. 9, Q04006. http://dx.doi.org/10.1029/2007GC001743.

Nagihara, S., Lister, C.R.B., Sclater, J.G., 1996. Reheating of old oceanic lithosphere: deductions from observations. Earth Planet. Sci. Lett. 139, 91–104.

Natarov, S.I., Conrad, C.P., 2012. The role of Poiseuille flow in creating depth-variation of asthenospheric shear. Geophys. J. Int. 190, 1297–1310.

Nettles, M., Dziewoński, A.M., 2008. Radially anisotropic shear-velocity structure of the upper mantle globally and beneath North America. J. Geophys. Res. 113, B02303. http://dx.doi.org/10.1029/2006JB004819.

Nicolas, A., Christensen, N.I., 1987. Formation of anisotropy in upper mantle peridotites; a review. In: Fuchs, K., Froidevaux, C. (Eds.), Composition, Structure and Dynamics of the Lithosphere–Asthenosphere System. In: Geodynamics, vol. 16. American Geophysical Union, Washington, DC, pp. 111–123.

Nishimura, C.E., Forsyth, D.W., 1989. The anisotropic structure of the upper mantle in the Pacific. Geophys. J. Int. 96, 203–229.

Podolefsky, N.S., Zhong, S., McNamara, A.K., 2004. The anisotropic and rheological structure of the oceanic upper mantle from a simple model of plate shear. Geophys. J. Int. 158, 287–296.

Ribe, N.M., 1989. Seismic anisotropy and mantle flow. J. Geophys. Res. 94, 4213–4223.

Ricard, Y., Vigny, C., 1989. Mantle dynamics with induced plate tectonics. J. Geophys. Res. 94, 17543–17559.

Ritsema, J., van Heijst, H., Woodhouse, J.H., 2004. Global transition zone tomography. J. Geophys. Res. 109, B02302. http://dx.doi.org/10.1029/2003JB002610.

Ritzwoller, M.H., Shapiro, N.M., Zhong, S., 2004. Cooling history of the Pacific lithosphere. Earth Planet. Sci. Lett. 226, 69–84.

Rychert, C.A., Shearer, P.M., 2009. A global view of the lithosphere–asthenosphere boundary. Science, 495–498.

Savage, M.K., 1999. Seismic anisotropy and mantle deformation: what have we learned from shear wave splitting? Rev. Geophys. 37, 65–106.

Schaeffer, A., Lebedev, S., 2013a. Global shear speed structure of the upper mantle and transition zone. Geophys. J. Int. 194, 417–449.

Schaeffer, A., Lebedev, S., 2013b. Global variations in azimuthal anisotropy of the Earth's upper mantle and crust (abstract). In: AGU Fall Meeting. Eos Trans. AGU. Abstract DI11A-2172.

Schmerr, N., 2012. The Gutenberg discontinuity: melt at the lithosphere–asthenosphere boundary. Science 335, 1480–1483.

Silver, P.G., 1996. Seismic anisotropy beneath the continents: probing the depths of geology. Annu. Rev. Earth Planet. Sci. 24, 385–432.

Smith, D.B., Ritzwoller, M.H., Shapiro, N.M., 2004. Stratification of anisotropy in the Pacific upper mantle. J. Geophys. Res. 109. http://dx.doi.org/10.1029/2004JB003200.

Song, T.-R.A., Kawakatsu, H., 2013. Subduction of oceanic asthenosphere: evidence from sub-slab seismic anisotropy. Geophys. Res. Lett. 39, L17301. http://dx.doi.org/10.1029/2012GL052639.

Tanimoto, T., Anderson, D.L., 1984. Mapping convection in the mantle. Geophys. Res. Lett. 11, 287–290.

Tanimoto, T., Anderson, D.L., 1985. Lateral heterogeneity and azimuthal anisotropy of the upper mantle: Love and Rayleigh waves 100–250 s. J. Geophys. Res. 90, 1842–1858.

Visser, K., Trampert, J., Kennett, B.L.N., 2008. Global anisotropic phase velocity maps for higher mode Love and Rayleigh waves. Geophys. J. Int. 172, 1016–1032.

Wessel, P., Smith, W.H.F., 1998. New, improved version of the Generic Mapping Tools released. Eos Trans. AGU 79, 579.

Xu, Y., Shankland, T.J., Linhardt, S., Rubie, D.C., Lagenhorst, F., Klasinsk, K., 2004. Thermal diffusivity and conductivity of olivine, wadsleyite and ringwoodite to 20 GPa and 1373 K. Phys. Earth Planet. Inter. 143, 321–336.

Yuan, K., Beghein, C., 2013. Seismic anisotropy changes across upper mantle phase transitions. Earth Planet. Sci. Lett. 374, 132–144.

Zhang, S., Karato, S.-i., 1995. Lattice preferred orientation of olivine aggregates deformed in simple shear. Nature 375, 774–777.

Supplementary material for "Origin of azimuthal seismic anisotropy in oceanic plates and mantle", *EPSL, 401*, 236-250, 2014

Thorsten W. Becker [a,*]

[a]*Department of Earth Sciences, University of Southern California, Los Angeles, CA*

Clinton P. Conrad [b]

[b]*University of Hawai'i at Manoa*

Andrew J. Schaeffer [c] and Sergei Lebedev [c]

[c]*Dublin Institute for Advanced Studies*

———

* Address: Department of Earth Sciences, University of Southern California, MC 0740, 3651 Trousdale Pkwy, Los Angeles, CA 90089–0740, USA. Phone: ++1 (213) 740 8365, Fax: ++1 (213) 740 8801

Email address: `twb@usc.edu` (Thorsten W. Becker).

This supplementary material for "Origin of azimuthal seismic anisotropy in oceanic plates and mantle" by Becker et al. (*Earth and Planetary Sciences*, doi:10.1016/j.epsl.2014.06.014, 2014) contains additional details including, 1), a description of the construction of the azimuthally anisotropic tomography model *SL2013SVA*, 2), visualizations and quantitative cross-model comparisons between different azimuthally anisotropic models, 3), a table with the best fit, ridge-fixed reference frame *RNR* plate motion Euler poles, 4), a discussion of the *LPO* model in light of net rotation akin to Becker (2008), and, 5), depth-dependent model misfit plots akin to Figure 5 of the main text for alternative tomography models.

Description of model *SL2013SVA*

In this section, we provide a brief summary of the *SL2013SVA* model (the details of which are the subject of a forthcoming paper) as analyzed in the main text. For more details on our multimode waveform methods, we refer the interested reader to Lebedev et al. (2005), Lebedev and van der Hilst (2008), and Schaeffer and Lebedev (2013a). *SL2013SVA* is the anisotropic component of the model *SL2013SV* (Schaeffer and Lebedev, 2013a), with the isotropic and anisotropic components computed simultaneously using the same dataset of 521,705 successfully fit, vertical-component, broadband seismograms. These half-million seismograms were selected from a master dataset of more than 750,000, recorded by more than 3000 seismometers belonging to international, national, regional, and temporary networks running from the 1990s until 2012. A mutually consistent subset was selected using outlier analysis (selecting ~522,000 from 750,000, as outlined in Schaeffer and Lebedev, 2013a). The total period range spans 11–450 s.

The inversion procedure is split into three steps. First we apply the Automated Multimode Inversion (AMI; Lebedev et al., 2005) to a dataset of more than 5 million vertical-component seismograms, each of which has been pre-processed, quality-controlled, and response-corrected to displacement. The initial dataset includes seismograms from all earthquakes in the CMT catalog (e.g. Ekström et al., 2012), including relatively small events recorded at long distances; low signal to noise ratios are the main reasons for the rejection of many seismograms by the waveform inversion procedure. The result of a successful waveform inversion is a set of linear equations with uncorrelated uncertainties that describe one-dimensional (1D) average perturbations in *S*- and *P*-wave velocity within approximate sensitivity volumes between each source-receiver pair, with respect to a 3D reference model (Lebedev and van der Hilst, 2008). In the second step, the equations generated by AMI are combined together into one large system and solved for the 3D distribution of *P* and *S* velocities, and 2Ψ *S*-wave azimuthal anisotropy (eq. 1 of the main text), as a function of depth, spanning the crust, upper mantle, transition zone and the upper part of the lower mantle. The inversion is carried out subject to regularization, consisting of lateral smoothing and gradient damping, vertical gradient damping, and

a minor degree of norm damping. The third step consists of a final outlier analysis of the dataset, from which an additional $\sim$3.5% of successful fits are removed *a posteriori*, leaving the most mutually consistent $\sim$511,000 to be re-inverted for the final model.

SL2013SVA is parameterized laterally on a global triangular grid of knots (Wang and Dahlen, 1995) with an approximate inter-knot spacing of 280 km (same as *SL2013SV*). Vertically, the model is parameterized using triangular basis functions centered at 7, 20, 36, 56, 80, 110, 150, 200, 260, 330, 410, 485, 585, 660, 810, and 1009 km depth (with pairs of half triangles for the transition zone discontinuities). The lateral smoothing parameters are larger for anisotropic terms (compared to isotropic), however, the vertical gradient damping and norm damping are equal. Additionally, path re-weighting is incorporated in order to reduce the effect of the many similar paths in the dataset. In Figure S1 we present five slices through *SL2013SVA* (left panels, a–e) at 75, 125, 175, 225, and 275 km depth, with comparisons to *DR2012* and *YB13SV* in the center and right panels.

Several tests were performed to verify the quality and robustness of *SL2013SVA*. First, we examined inversions both with and without the inclusion of azimuthally anisotropic terms. Comparison of the resulting isotropic models are qualitatively identical (no change to the interpretation). Visually, the largest changes were in the depth range 50–150 km depth in the Pacific Ocean basin; the addition of anisotropic terms results in a reduction of small-scale isotropic heterogeneity. Quantitatively, the addition of anisotropy results in the largest change in isotropic RMS of 15 m/s, at 100 km depth. An even smaller change of $\sim$10 m/s is observed at 150 and 200 km depth; at greater depths the isotropic RMS of both models is within 3–4 m/s ($<$0.1% difference). Secondly, we tested the sensitivity to the chosen vertical gradient damping. Results demonstrate that the anisotropy orientations are largely insensitive to the degree of vertical gradient damping. Model *SL2013SVA2* as shown in Figure S2b, for example, has no vertical gradient damping and is correlated with *SL2013SVA* at the $r_{20} = 0.99$ level on average over the upper 350 km of the mantle.

Additional synthetic tests were carried out to ensure minimal cross-contamination between model parameters (*i.e.*, leakage of isotropic structure into anisotropic, and *vice versa*). Two synthetic datasets were generated through matrix multiplication of the design ("*A*") matrix of *SL2013SVA* (and *SL2013SV*) with two different synthetic models: only the isotropic terms of *SL2013SV* (anisotropy set to zero) and only the anisotropic terms of *SL2013SVA* (isotropic set to zero). The synthetic datasets were inverted using the same parameters as those in the generation of *SL2013SVA* (and *SL2013SV*). Examination of the resulting models confirms the independence of the isotropic and anisotropic terms; $<$0.5% azimuthal anisotropy amplitudes are observed with *SL2013SV* as input, and similarly $\sim$ 1% maximum amplitudes in isotropic velocity for *SL2013SVA* as input.
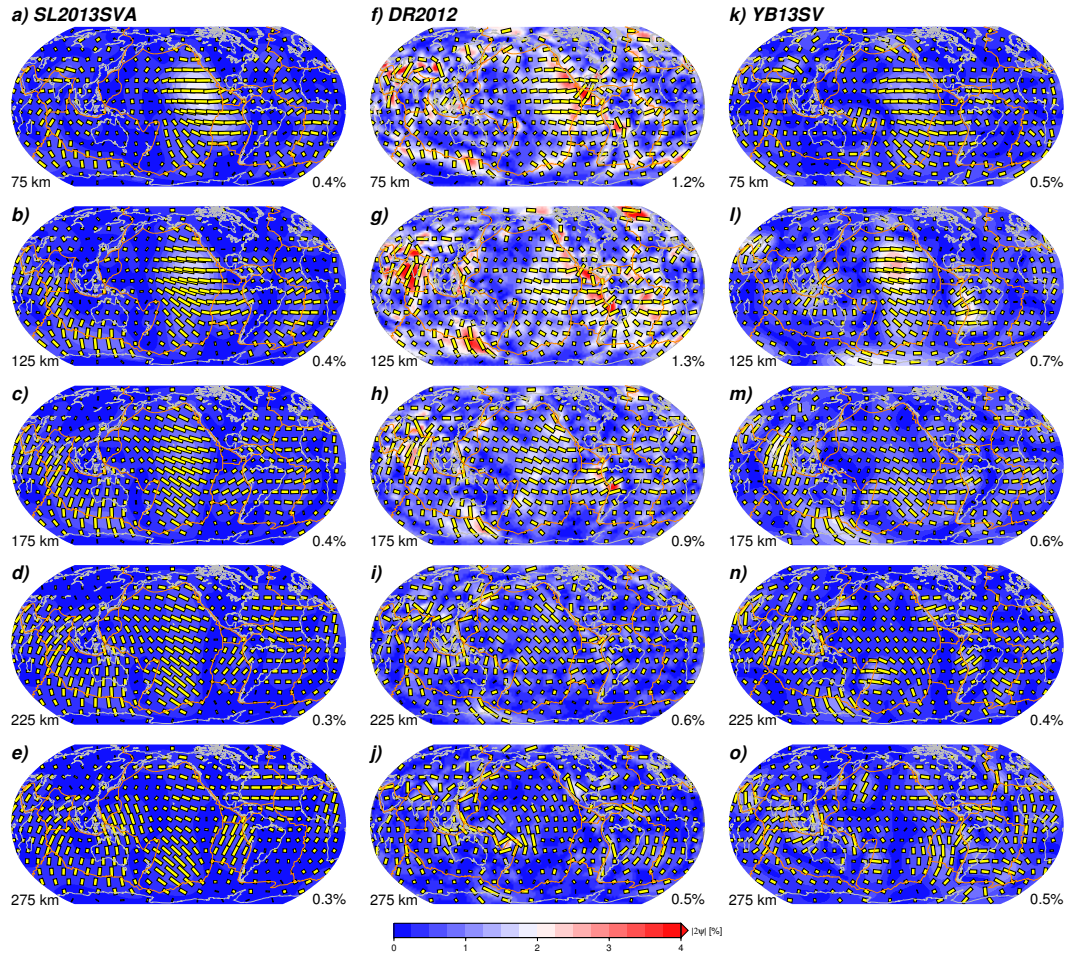
3

Fig. S1. Comparison of azimuthal anisotropy throughout the uppermost mantle from *SL2013SVA* (a-e, Schaeffer and Lebedev, 2013b), *DR2012* (f-j, Debayle and Ricard, 2013), and *YB13SV* (k-o, Yuan and Beghein, 2013), at the indicated depth levels. Sticks indicate the fast propagation orientation (Ψ), normalized to the maximum at each depth. Colored background indicates the amplitude of anisotropy, $|2\Psi| = \sqrt{A_1^2 + A_2^2}$ (eq. 1 of the main text), with legend on lower right indicating the mean amplitude for each layer.

Radial correlation, cross-model correlation, and RMS of azimuthally anisotropic tomography models

We here provide some additional analysis of the character of the three different seismological models of upper mantle azimuthal anisotropy that were considered in the main text: *SL2013SVA* by Schaeffer and Lebedev (2013b) and as described above, *DR2012* by Debayle and Ricard (2013), and *YB13SV* by Yuan and Beghein (2013). The anisotropic patterns of these models are plotted for upper mantle depths in Figure S1. To further analyze the models, we expand the azimuthal anisotropy signal into generalized spherical harmonics as detailed in Becker et al. (2007).

We show radial correlation functions in Figure S2; those quantify the depth range
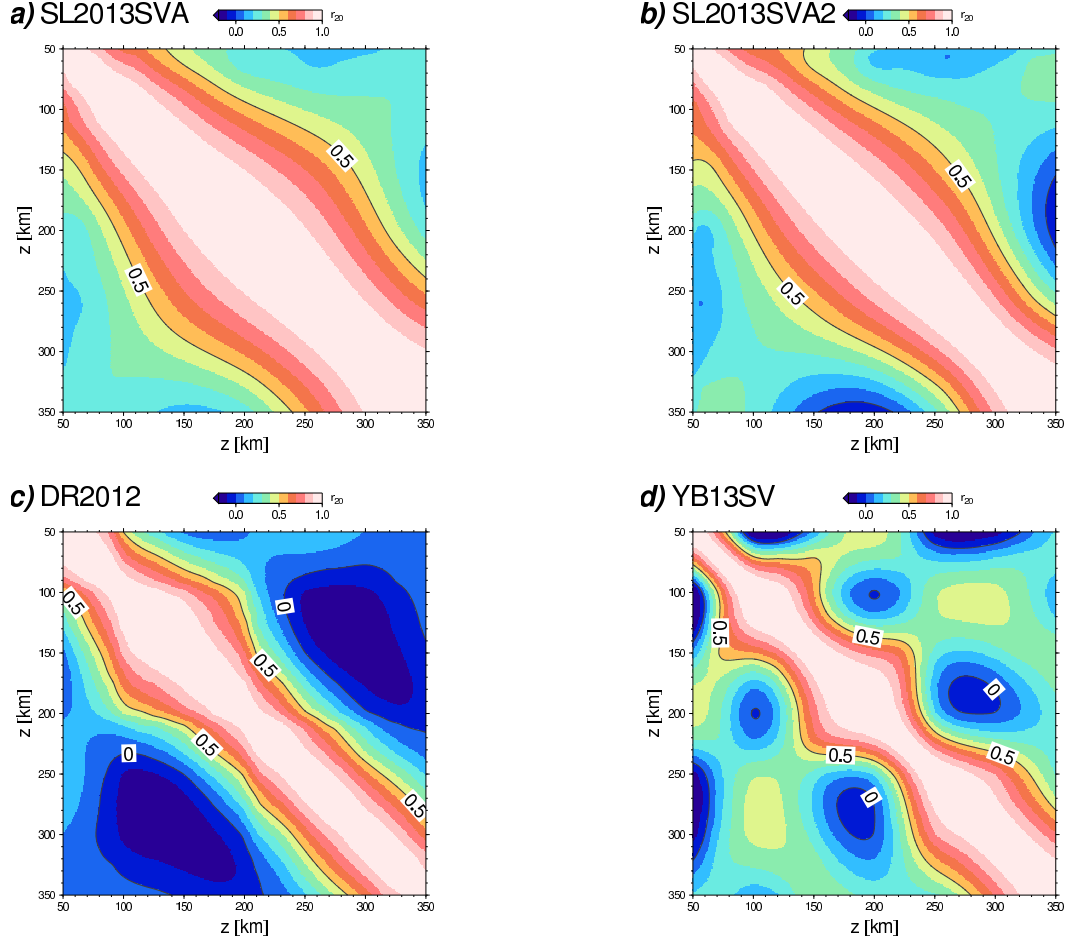
Fig. S2. Radial correlation functions for azimuthal anisotropy (2Ψ signal) of the three seismological models considered in the main text (a, c, and d; cf. Figure S1) based on generalized spherical harmonic expansion up to degree 20. Model *SL2013SVA2* is a test case using the same approach as in *SL2013SVA*, but applying no vertical damping.

over which structure is coherent, at each depth (e.g. Tackley et al., 1994; Puster and Jordan, 1997; Becker and Boschi, 2002). Figure S2 is based on total correlation up to degree L, r_L, with $L = 20$. It is clear that *SL2013SVA* is indeed very vertically smooth (by design), and *DR2012* lies intermediate between *SL2013SVA* and *YB13SV*, which allows for the most rapid variations of anisotropy with depth, as discussed by Yuan and Beghein (2013).

As *SL2013SVA* appears more vertically smooth than *DR2012* and *YB13SV*, we have conducted tests exploring the effect of the vertical gradient damping employed in generating *SL2013SVA*. A reduction in the vertical damping coefficients by several orders of magnitudes, compared to *SL2013SVA*, or even a complete removal of vertical smoothing, as for *SL2013SVA2* in Figure S2b, does not significantly affect the patterns of fast azimuths, which remain nearly unchanged at each depth, while the amplitudes are somewhat enhanced. We therefore think that the analysis presented in the main text is not adversely affected by undue structure due to smoothing.

5

Figure S3 explores the similarity in terms of anomaly patterns for the three seismological models. We compute cross-correlation, r_L, as a function of depth, depth-averages thereof, $\langle r_L \rangle$, and the RMS power. As was discussed by Becker et al. (2007) for phase velocity maps of azimuthal anisotropy, there are quite large differences in amplitude and patterns between models. That said, compared to the earlier analysis of phase velocity similarity, the newer 2Ψ models show $\langle r_8 \rangle$ correlation values that are larger than the old ones by ~ 0.2, though still not close to the similarity of imaged isotropic *SV* structure, as expected. While all models agree in that most azimuthal anisotropy is focused in the upper ~ 350 km of the mantle, actual amplitudes of $|2\Psi|$ are still different by factors of ~ 5 in some depth ranges, and there are no consistent finer detail variations of RMS with depth, as expected from Figure S2.

However, as noted in the main text, it appears that the model on which we focus here, *SL2013SVA*, is more similar to the other two models, *DR2012* and *YB13SV* than they are to each other, based on the pattern match shown by average cross correlations. This might indicate that *SL2013SVA*, which is quite smooth compared to the other models (cf. Figure S1), captures the long wavelength structure of average anisotropy well, even if finer-scale structure, such as rapid changes of anisotropy with depth (Figure S2, cf. Yuan and Beghein, 2013) are less well resolved by Schaeffer and Lebedev's (2013b) model.

Best fit, ridge-fixed reference frame APM model *RNR*

For completeness, Table S1 provides the individual plate Euler poles for the *RNR* APM model we introduce in the main text based on minimizing the global motion of ridges. The model is identical to NUVEL-1A (DeMets et al., 1994) besides its net rotation component intended to minimize ridge motions, at a rate of 0.16°/Myr with an Euler pole at 22°E/82°S relative to NNR.

***LPO* model match as a function of net rotation**

Figure S4 reproduces the analysis of Becker (2008) (his Figure 2) for the more recent, azimuthally anisotropic tomographic models *SL2013SVA* (Schaeffer and Lebedev, 2013b), *DR2012* (Debayle and Ricard, 2013), and *YB13SV* (Yuan and Beghein, 2013) as considered in the main text. We show the match between tomography and *LPO* based on mantle flow computations that have varying degrees of net rotation of the lithosphere with respect to the lower mantle, from no net rotation (NNR) to the large net rotation found in HS3 (Gripp and Gordon, 2002). The metrics shown in Figure S4 are correlation, as computed for generalized spherical
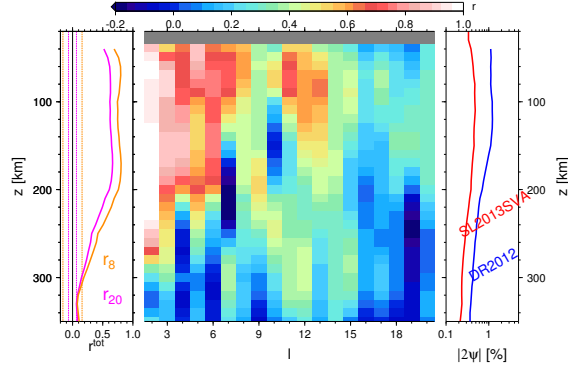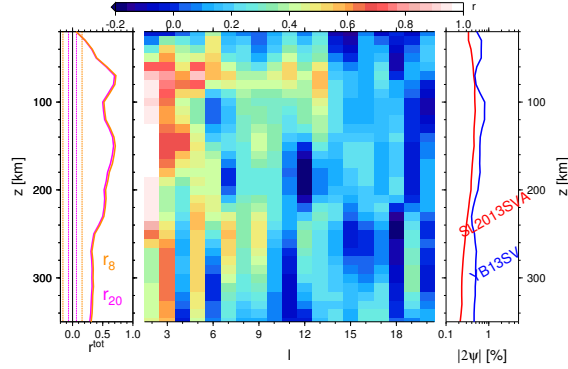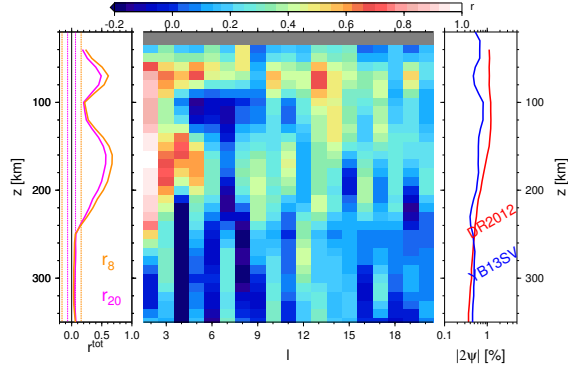
Fig. S3. Cross-model correlation and power for azimuthal anisotropy from seismology for uppermost mantle depths for the three models considered in the main text (cf. Figure S1). The 2Ψ signal has been expanded into generalized spherical harmonics (cf. Becker et al., 2007) up to degree $\ell_{max} = 20$. Left plot shows total correlation up to degrees $L = 8$ and 20, r_8 and r_{20}, respectively, with depth, z (orange and magenta solid lines, with depth-averaged values, $\langle r_L \rangle$, given in the title), and the corresponding 95% confidence range from Student's t test (dashed lines). Center plot shows correlation as a function of ℓ and z, and rightmost plot shows the RMS heterogeneity on a log-scale.

Table S1

Euler vectors for each plate, $\vec{\omega}$, for the *RNR*, "ridge-fixed" APM model. The net rotation of this model with respect to NUVEL-1A (DeMets et al., 1994) in a no net rotation reference frame is $\vec{\omega}_{NR} = \{0.02056, 0.0083, -0.1583\}$, corresponding to 21.9451°E, 82.0136°S at a rate of 0.1599°/Myr; else, *RNR* is identical to NNR NUVEL1A. All Euler vectors are given in a $\{x, y, z\}$ Cartesian (East, North, Up) reference frame in units of °/Myr.

plate	ω_x	ω_y	ω_z
Africa	0.0713	−0.1693	0.0663
Antarctica	−0.0268	−0.0892	0.0539
Arabia	0.4033	−0.0216	0.2289
Australia	0.4694	0.3019	0.2015
Caribbean	0.0100	−0.1857	−0.0679
Cocos	−0.5771	−1.2296	0.4675
Eurasian	−0.0360	−0.1289	0.0222
India	0.4024	0.0106	0.2306
Juan de Fuca	0.3067	0.4672	−0.4386
North America	0.0350	−0.1979	−0.1672
Nazca	−0.0675	−0.4831	0.3921
Pacific	−0.0663	0.2856	−0.7297
Philippine Sea	0.5983	−0.4020	−0.7297
South America	−0.0392	−0.0785	−0.2083

harmonics up to degree $\ell = 20$ (cf. Becker et al., 2007) and mean, angular orientational misfit, $\langle \Delta \alpha \rangle$, as in Figure 5 of the main text. The inferences drawn by Becker (2008) based on older azimuthal anisotropy models, that only moderate amounts of net rotation appear consistent with seismic anisotropy, are confirmed by the results in Figure S4.

Global depth dependence of geodynamic model misfit with azimuthal anisotropy for alternative tomography models

Figures S5 and S6 reproduce the global angular misfit as a function of depth plots discussed and presented in the main text for *SL2013SVA* (Schaeffer and Lebedev, 2013b) (Figure 5) for the alternative seismological models of azimuthal anisotropy from Debayle and Ricard (2013) (*DR2012*) and Yuan and Beghein (2013) (*YB13SV*).
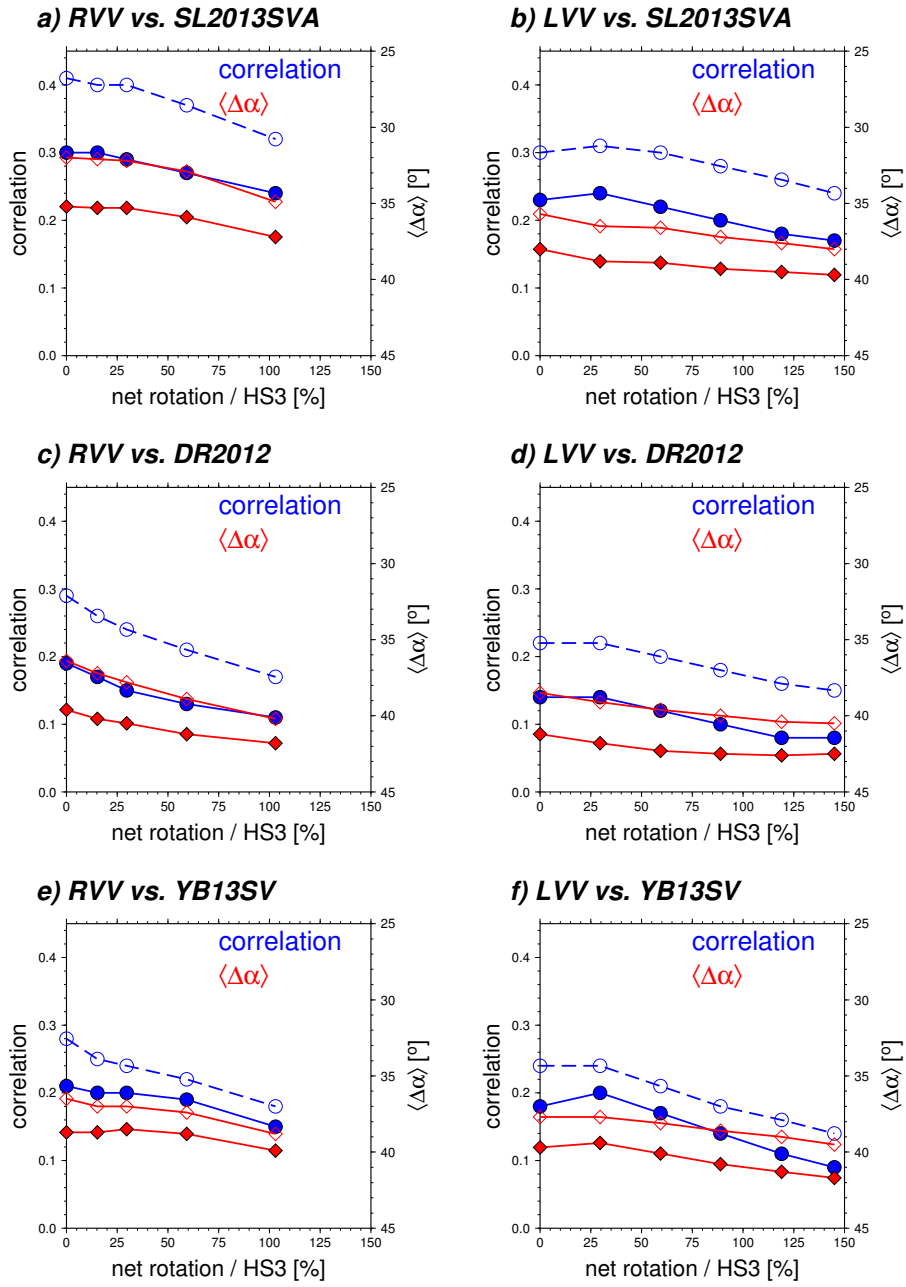
8

Fig. S4. Comparison of azimuthal anisotropy from tomography with *LPO* as predicted from mantle flow models with different degrees of net rotation of the lithosphere, expressed as fractions of HS3 (Gripp and Gordon, 2002). Results are from computations with only radial (a, c, e) and lateral viscosity variations (b, d, f), referenced to *SL2013SVA* (a, b), *DR2012* (c, d), and *YB13SV* (e, f). Solid and open symbols are for global metrics and when confined to oceanic plates only, respectively, and we show correlation computed from generalized spherical harmonics up to degree $\ell = 20$ and mean, angular orientational misfit, $\langle \Delta \alpha \rangle$. Figure is analogous to Figure 2 of Becker (2008), see there for details.
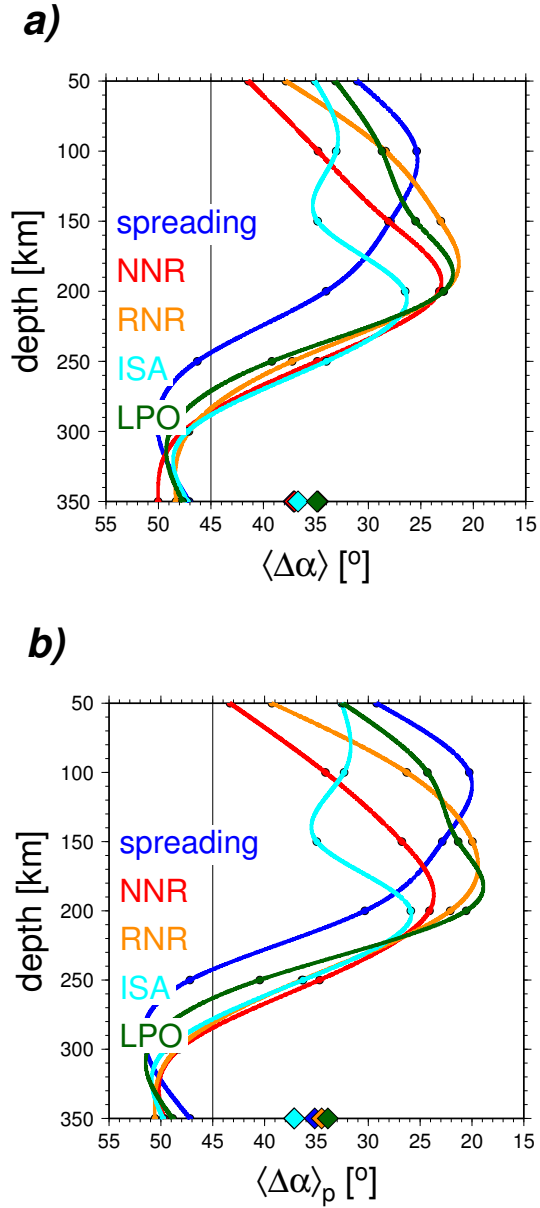
9

Fig. S5. a) Depth-dependence of global mean angular misfit, $\langle\Delta\alpha\rangle$, weighted by tomography anomaly amplitude, with azimuthal anisotropy in oceanic plates from *DR2012* (Debayle and Ricard, 2013) (see Figures 5 and S6 for other models). b) Depth dependence of misfit when computed weighing all oceanic basins evenly, $\langle\Delta\alpha\rangle_p$. Geodynamic models projected downward are paleo-spreading as well as APM models *NNR* and *RNR*. Depth–variable models based on mantle flow considered are *ISA* (Conrad and Behn, 2010) and *LPO* (Becker et al., 2008). Diamonds denote averages over the 50–350 km depth range for each model, as in Figure 5.
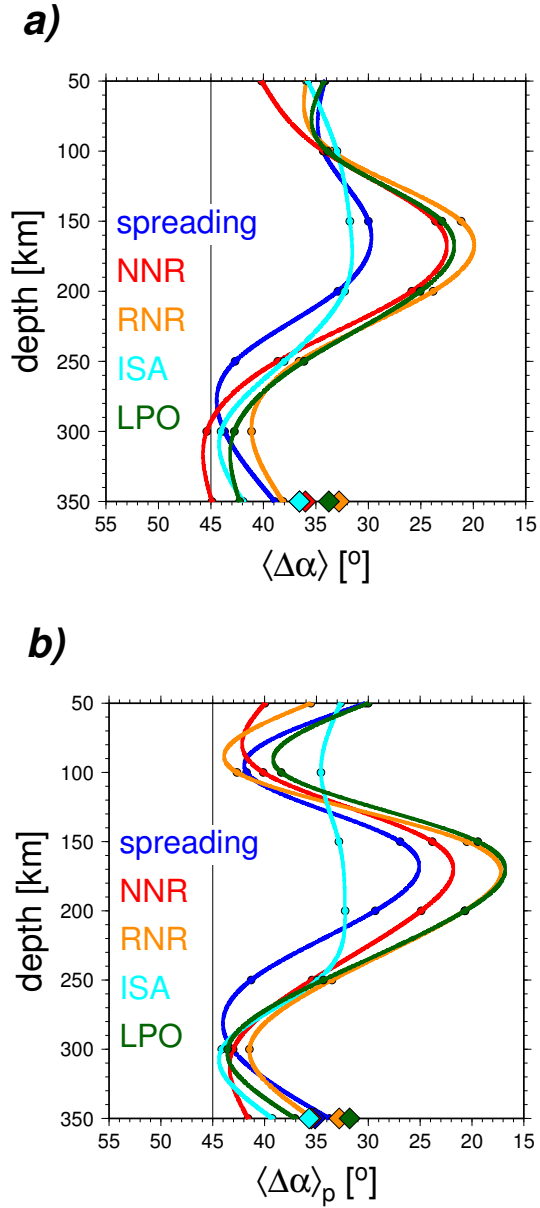
a)

b)

Fig. S6. a) Depth-dependence of global mean angular misfit, $\langle\Delta\alpha\rangle$, weighted by tomography anomaly amplitude, with azimuthal anisotropy in oceanic plates from *YB13SV* (Yuan and Beghein, 2013) (see Figure 5 and S5 for other models). b) Depth dependence of misfit when computed weighing all oceanic basins evenly, $\langle\Delta\alpha\rangle_p$. Geodynamic models projected downward are paleo-spreading as well as APM models *NNR* and *RNR*. Depth-variable models based on mantle flow considered are *ISA* (Conrad and Behn, 2010) and *LPO* (Becker et al., 2008). Diamonds denote averages over the 50–350 km depth range for each model, as in Figure 5.

References

Becker, T. W., 2008. Azimuthal seismic anisotropy constrains net rotation of the lithosphere. Geophys. Res. Lett. 35, L05303. doi:10.1029/2007GL032928. Correction: doi:10.1029/2008GL033946.

Becker, T. W., Boschi, L., 2002. A comparison of tomographic and geodynamic mantle models. Geochem., Geophys., Geosys. 3, 1. doi:10.1029/2001GC000168.

Becker, T. W., Ekström, G., Boschi, L., Woodhouse, J. W., 2007. Length-scales, patterns, and origin of azimuthal seismic anisotropy in the upper mantle as mapped by Rayleigh waves. Geophys. J. Int. 171, 451–462.

Becker, T. W., Kustowski, B., Ekström, G., 2008. Radial seismic anisotropy as a constraint for upper mantle rheology. Earth Planet. Sci. Lett. 267, 213–237.

Conrad, C. P., Behn, M., 2010. Constraints on lithosphere net rotation and asthenospheric viscosity from global mantle flow models and seismic anisotropy. Geochem., Geophys., Geosys. 11, Q05W05. doi:10.1029/2009GC002970.

Debayle, E., Ricard, Y., 2013. Seismic observations of large-scale deformation at the bottom of fast-moving plates. Earth Planet. Sci. Lett. 376, 165–177.

DeMets, C., Gordon, R. G., Argus, D. F., Stein, S., 1994. Effect of recent revisions to the geomagnetic reversal time scale on estimates of current plate motions. Geophys. Res. Lett. 21, 2191–2194.

Ekström, G., Nettles, M., Dziewónski, A. M., 2012. The global CMT project 2004-2010: Centroid-moment tensors for 13,017 earthquakes. PEPI 200-201, 1–9.

Gripp, A. E., Gordon, R. G., 2002. Young tracks of hotspots and current plate velocities. Geophys. J. Int. 150, 321–361.

Lebedev, S., Nolet, G., Meier, T., van der Hilst, R. D., 2005. Automated multimode inversion of surface and S waveforms. Geophys. J. Int. 162, 951–964.

Lebedev, S., van der Hilst, R. D., 2008. Global upper-mantle tomography with the automated multimode inversion of surface and S-wave forms. Geophys. J. Int. 173, 505–518.

Puster, P., Jordan, T. H., 1997. How stratified is mantle convection? J. Geophys. Res. 102, 7625–7646.

Schaeffer, A., Lebedev, S., 2013a. Global shear speed structure of the upper mantle and transition zone. Geophys. J. Int. 194, 417–449.

Schaeffer, A., Lebedev, S., 2013b. Global variations in azimuthal anisotropy of the Earth's upper mantle and crust (abstract). Eos Trans. AGU , DI11A–2172AGU Fall Meeting Abstract volume.

Tackley, P. J., Stevenson, D. J., Glatzmaier, G. A., Schubert, G., 1994. Effects of multiple phase transitions in a three-dimensional spherical model of convection in Earth's mantle. J. Geophys. Res. 99, 15,877–15,901.

Wang, Z., Dahlen, F. A., 1995. Spherical-spline parameterization of three-dimensional Earth models. Geophys. Res. Lett. 22, 3099–3102.

Yuan, K., Beghein, C., 2013. Seismic anisotropy changes across upper mantle phase transitions. Earth Planet. Sci. Lett. 374, 132–144.